Molecular Mechanisms of OER for Artificial Photosynthesis

Subjects: Chemistry, Applied

Contributor: Yoshio Nosaka

Addressing the global environmental problem of water splitting to produce hydrogen fuel by solar energy is receiving so much attention. In water splitting, the essential problem to solve is the development of efficient catalysts for oxygen production. In the generation of hydrogen by water splitting, molecular oxygen should be evolved at the same time. However, it is not so easy to artificially achieve photosynthetic oxygen generation by developing novel systems in a short period of time, which took one billion years in the natural world. The oxidation of water to produce oxygen, i.e., oxygen evolution reaction (OER), involves transfers of four electrons and four protons, while the reduction of water to produce hydrogen, i.e., hydrogen evolution reaction (HER), is a reaction of two electrons and two protons.

oxygen evolution reaction catalysis mechanism artificial photosynthesis titanium oxide bismuth vanadate metal oxides Fourier transform infrared spectroscopy density functional theory metal oxide

1. TiO_2

There are abundant reports in which molecular mechanisms of OER at the TiO_2 surface could be found. Research progress in the theoretical calculations for water splitting with TiO_2-based photocatalysts were also reported [1][2]. Most of the theoretical calculations were performed for rutile (110) and (001) surfaces. Recently, the rutile (100) surface was investigated for OER activity assuming the AEM process [3]. However, it has been shown experimentally that rutile powder consists of (110) and (011) or equivalent surfaces, and reduction occurs at the (110) surface while oxidation occurs at the (011) surface. Though the anatase (101) surface is also used in the theoretical calculation, many experimental observations have indicated that rutile TiO_2 is more active for OER than anatase TiO_2 [4][5]. This experimental conclusion could be explained by the authors as the surface Ti_{5C}-Ti_{5C} distance of rutile is shorter than that of anatase [6], and the recent theoretical calculation supported this explanation by comparing the anatase (101) surface with the rutile (110) surface [7].

In researchers' report, a molecule $Ti_5O_{19}H_{16}$ modeling rutile (011) surface was used to investigate the OER process [8]. As the result of the total energy calculation, surface Ti_{5C} which can be coordinated by H_2O could make a hydrogen bonding with the facing bridged O atom. As shown in **Figure 1**, the first hole attacks the bridge O and then moves to the hydrogen bonding H_2O molecule to form Ti-O• at the facing Ti_{5C} which is the adsorbed OH radical. The second hole can attack Ti-O• or bridged O again to generate OH radical combined with Ti-O•, resulting in the formation of Ti-OOH species. This adsorbed hydroxyperoxo could be stabilized by forming a Ti-OO-Ti structure with another facing Ti_{5C} at the (011) surface. This calculation result suggested that the surface three Ti atoms concerning the OER process are not laid on a line but the third Ti of Ti_{5C} should be facing the bridged O [8].

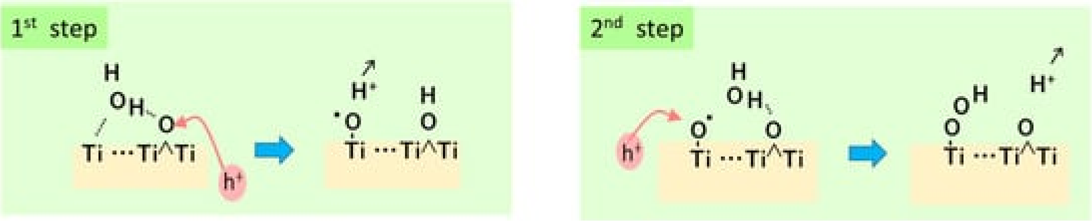

Figure 1. Key steps in water oxidation deduced from a DFT calculation for the model molecule of rutile TiO_2(011) surface. Reproduced from *Catalysts* **2022** [8] under the license of CC BY 4.0 from MDPI publishers.

Two decades ago, Nakamura et al. reported a molecular mechanism of water oxidation at rutile powder as shown in **Figure 2** [9][10], their reports were referred to in the discussion. In his mechanism, three-coordinated bridging O at a step or kink of the surface is attacked by a hole, simultaneously, WNA takes place to form Ti-O•, and then a pair of Ti-O• generate Ti-OO-Ti structure, and it becomes Ti-OOH [10].

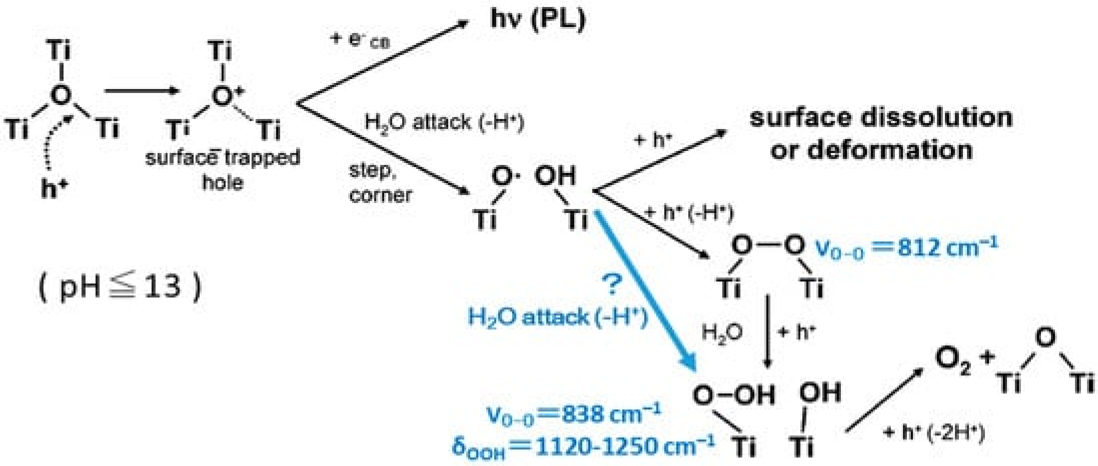

Figure 2. Oxygen generation mechanism suggested by Nakamura et al. Blue arrow was added by the present author. Reproduced from *J. Am. Chem. Soc.* **2005** [10] with permission from the American Chemical Society.

The molecular mechanism in **Figure 2** was obtained by the observations with the ATR-FTIR for rutile powder and the STM and photoluminescence for rutile single crystals of (100) and (110) facets. The assignment of FTIR spectra was performed for photoinduced O_2 reduction under irradiation based on the isotope effect using D_2O and $H_2{}^{18}O$ [11]. The signal assignment seems reasonable, and the isotope effect is well simulated. In the calculation, the signal intensity for bending mode δ(OOH) is larger than that of the stretching mode ν(OO), and the signal of the bending mode was clearly shown in the report [11]. However, in the in situ FTIR spectra for water oxidation, the signal at larger than 1100 cm^{-1} in the spectrum was not shown [9]. The spectrum measured in $H_2{}^{18}O$ did not show the spreading near 1100 cm^{-1}. Since many chemical species have signals around 838 cm^{-1}, the observation of Ti-OOH in the experiment may have some problems.

Having consensus on the assumption that the first oxidation takes place at bridged oxygen Ti-O-Ti, the reaction mechanism of OER was discussed [4]. Recently, Zhuang and Cheng [12] reported that at the rutile (110) surface, pKa of $Ti_{5C}OH_2$ is larger than that of $Ti_{5C}OH$-, and then the coordination structure $Ti_{5C}O^{2-}$ exists stably in water and easily becomes Ti-O•. These results in the calculation seem to contradict the fact that the isoelectric point of rutile TiO_2 is around pH 6. The rutile (110) is not a minor surface in rutile powder as described above. It should be noted that theoretical calculations can bring the result without exception on the basis of the assumed model regardless of the experimental reality. Therefore, it should be careful to refer to the molecular mechanism derived only from the theoretical calculations. Thus, the calculation methods should be used only for the case justified with the experimental results.

2. $BiVO_4$

$BiVO_4$ was discovered first as the semiconductor photocatalyst to have the ability of water oxidation with visible light and the developed process was compiled in the report by Kudo et al. [13]. As the oxygen evolution photocatalysts, Mo-doped $BiVO_4$ embedded into an Au layer was employed in a Z-scheme photocatalytic system to exhibit 1.1% STH efficiency [14]. Aiming for utilization in photocatalytic oxidation, there are many reports that describe the effects of surface crystalline systems, morphologies, hetero junctions, and so on [15].

The electrochemical impedance technique was applied to investigate the micro kinetics at $BiVO_4$ photoelectrode and found the long-lived holes (0.1–1 s). Two kinds of recombination paths were suggested; one is the fast recombination with photogenerated electrons, and another is the recombination with $BiVO_4$ bulk electrons [16]. By measuring the lifetime of the photoluminescence, the recombination was found to occur in nanoseconds, which is probably caused by the multiphonon transition with deep-energy defects [17]. Sub-bandgap is formed by the V-deficiency to accelerate the recombination rate [18].

To understand the reaction mechanism, there are many computational studies in the literature. Walsh et al. concluded that the valence band (VB) of O_{3p} is coupled with Bi_{6s} to raise the VB maximum, while the conduction band (CB) consists of V_{3d} and O_{2p} and Bi_{6p}. Therefore, the adsorption of ROS is expected to take place at the Bi site [19]. On the other hand, in a later report for the (010) surface, O vacancy provides the V site as an active site. That is, the presence of the O vacancy increased the adsorption energy of H_2O, OH, O•, and the calculated free energy showed a decrease in the barrier for spontaneous charge transfer to electrolyte [20]. The doping of Co^{2+} was replaced with Bi^{3+}, forming an O vacancy, and H_2O was replaced with the vacancy, which has been calculated to cause a decrease in the free energy by −0.28 eV [21]. At the (001) surface without vacancy, OH radical is easily formed, on the other hand at the (101) surface, where vacancies are generated by Mo/W doping, strong charge transfer to oxidation intermediates in OER takes place. This difference in the surface character causes charge transfer between (101) and (001) surfaces [22]. For the (010) surface, surface O vacancy is important to the adsorption of water in the catalytic activity [23]. The effect of O vacancy at the subsurface on the charge accumulation in the OER process was investigated. As a result, the O vacancy does not affect the photon acquisition or energy transportation in the crystal [24].

Twin-structured $BiVO_4$ was examined in the energy calculation [25]. The structure of the rate-determining step was considered with energy calculations in the OER process for four models (two AEM and two LOM). It was concluded that a larger amount of the twin structure causes a high OER activity [25].

Nikacevic et al. theoretically suggested some routes of OER at the $BiVO_4$ surface as shown in **Figure 3**. At the (001) surface, 97% of vacancies are coordinated with water. As shown in pathway A in this figure, Bi-OO-V is formed as an intermediate, and O_2 is evolved. On the other hand, only 0.05% of the O vacancy at the (011) surface was coordinated with water, but as shown in pathway B, through the Bi-OOH structure, O_2 is evolved as OER pathway B with a byproduct of H_2O_2 as the HPER pathway [26].

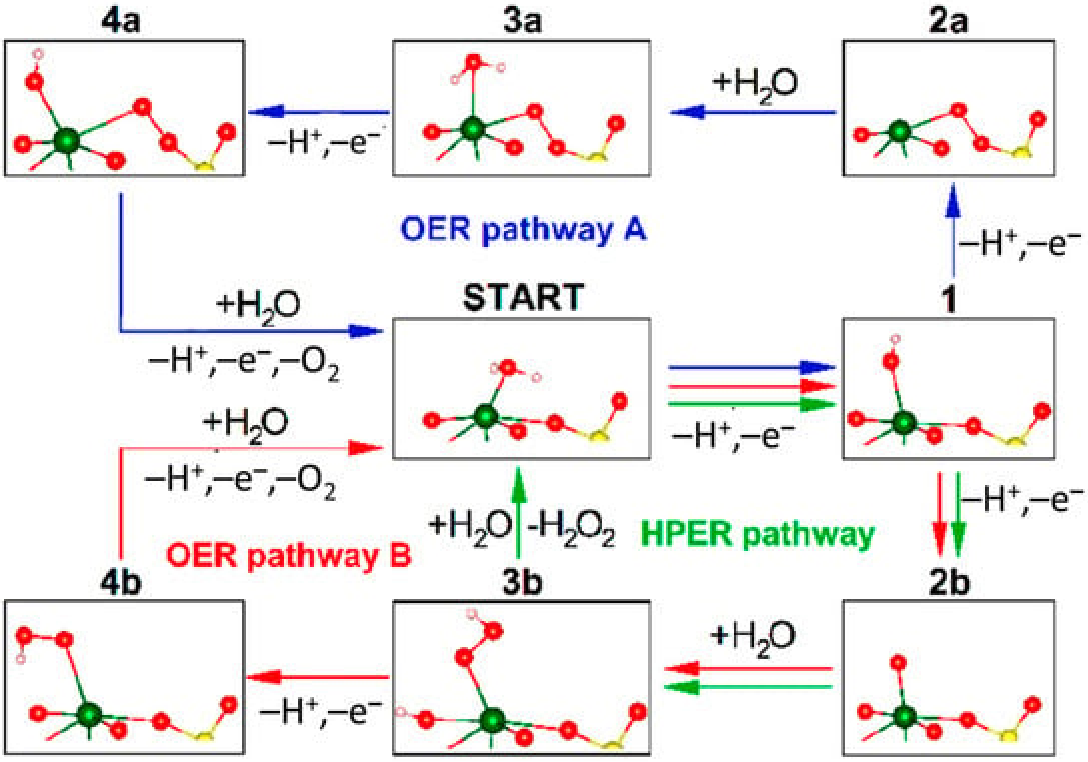

Figure 3. Suggested pathways deduced from DFT calculations for oxygen evolution reaction (OER) and hydrogenperoxide evolution reaction (HPER). Reproduced from *ACS Catal.* **2021** [26] with permission from the American Chemical Society.

In the experimental research for the molecular mechanism of the $BiVO_4$ OER process, the surface interrogation scanning electrochemical microscopy technique was applied to W/Mo-doped $BiVO_4$ electrodes [27]. In this report, the generation of the OH radical was at the ratio of 6% of the absorbed photons in the OER process [27]. However, they detected the OH radical by the oxidation of $IrCl_6^{2-}$ for electrochemical monitoring. For non-doped $BiVO_4$ electrodes, Nakabayashi et al. detected the OH radical by trapping it with a fluorescent reagent and reported that the yield of the OH radical was 0.06% of the photocurrent while almost 100% was used to generate molecular oxygen [28]. FTIR spectra under light irradiation were measured for the $BiVO_4$ photoanode [29]. The in situ FTIR spectra measured in $H_2{}^{18}O$ and D_2O are compiled in **Figure 4**. To analyze the isotope shift, DFT calculation with the B3LYP/LanL2DZ method in Gausian03W was performed for model molecule $(OH)_4Bi\text{-}OOH$. When the calculated isotope shift was checked with the measured FTIR spectra in the literature [29], the reported assignment of the peak in D_2O was found to be incorrect. The peak positions of δ(OOD) and ν(OO) should be alternated in D_2O. Then, the large isotope shift in $H_2{}^{18}O$ shows that both O in Bi-OOH originated from water and that the lattice oxygen of $BiVO_4$ was not contained in the OER process. Thus, experimental observations of the presence of Bi-OOH and the 100% yield of the O_2 show that the OER pathway B in **Figure 3** is purely the molecular mechanism of OER at the $BiVO_4$ photoanode.

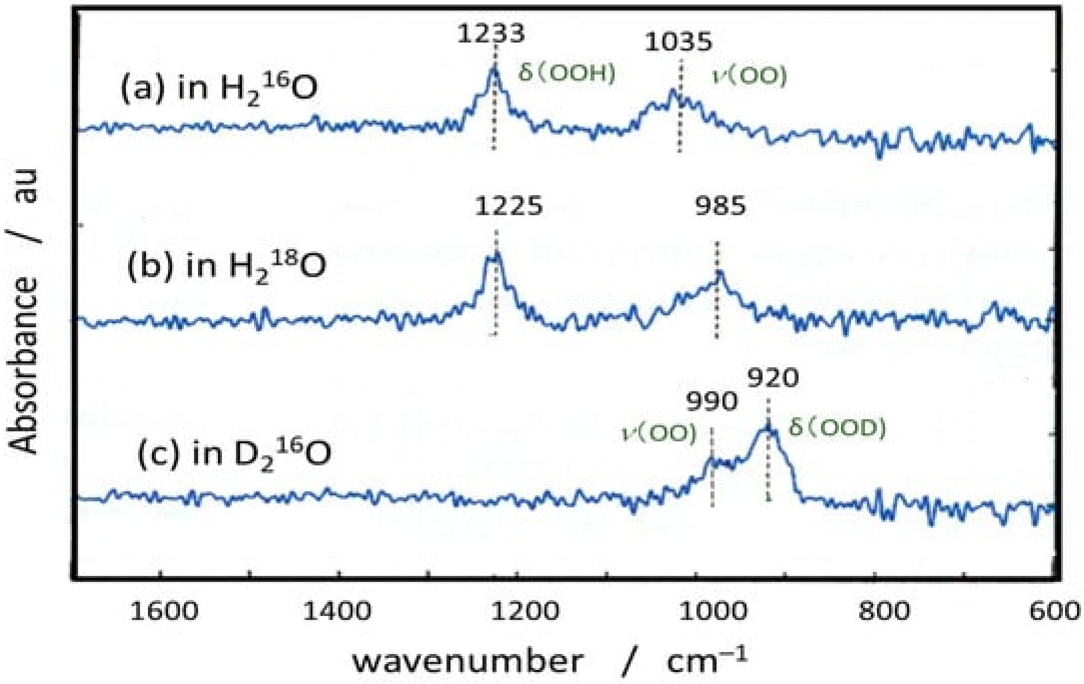

Figure 4. ATR-FTIR spectra of $BiVO_4$ photoanode under light irradiation in (**a**) normal water, (**b**) O-18 labeled water, and (**c**) heavy water. Compiled from the figures in Ref [29]. Reproduced from *J. Phys. Chem. C* **2021** [29] with permission from the American Chemical Society.

Though OER catalytic activity is observed for photoanode, to increase the separation of charges, $BiVO_4$ photoanode is sometimes used with the deposition of some OER catalysts such as Fe-OOH [30], CoPi [31], and Co_3O_4 [32].

3. $SrTiO_3$

Strontium titanate ($SrTiO_3$) is a well-documented photocatalyst in both one-step and two-step (Z-scheme) water-splitting systems as first reported in 1980 [33]. By using an ultrafast sub-band-gap probe with white light and 400 nm beam on $SrTiO_3$, one-electron intermediates were identified to be radicals located in Ti–O• (oxyl) and Ti–O•–Ti (bridge) groups with the initial radical formation time of 1.3 ps as shown in **Figure 5** [34]. After photo-triggering the water oxidation reaction from the Nb-doped n-$SrTiO_3$ surface, the microsecond decay of the intermediates affirms transition-state theory through two distinct time constants. The reaction conditions can be adjusted to allow selection between the two pathways, one characterized by a labile intermediate facing the electrolyte (the oxyl), and the other by a lattice oxygen (the bridge) [35]. Picosecond optical spectra of the Ti-OH population on lightly doped $SrTiO_3$ are ordered by the surface hydroxylation. A Langmuir isotherm as a function of pH extracted an effective equilibrium constant relatable to the free energy difference of the first oxygen evolution reaction step [36].

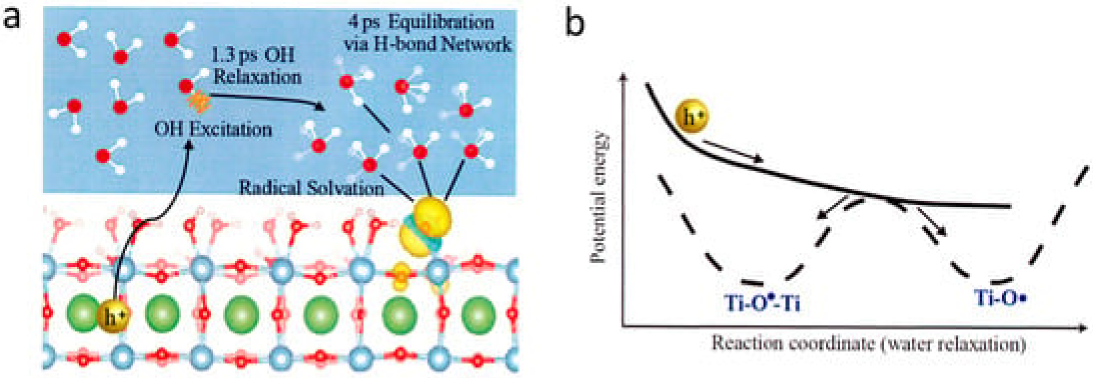

Figure 5. Initial step of photocatalytic OER at $SrTiO_3$/water interface. (**a**) OH vibration energy relaxed by H-bond network. (**b**) Proposed reaction diagram of forming two kinds of surface radicals. Reproduced from *J. Am. Chem. Soc.* **2017** [34] with permission from the American Chemical Society.

Single crystalline $SrTiO_3$ photoanodes were irradiated with a focused laser to spatially define the degradation. By characterizing the degradation using optical spectroscopy and electron microscopy, the material dissolution constitutes an upper bound of 6% of the charge passed in a pH 13 electrolyte, while for pH 7, it reaches 23%; the pH dependence is anti-correlated with the ultrafast population of trapped charge. Since the dominant lattice dissolution reaction that occurred was thermodynamically concomitant with the OER, the reaction mechanism in Ref [35] was not supported, though the photon flux seems very high in this experiment [37].

4. Ga_2O_3

On Ga_2O_3-based photocatalysts, the overall water-splitting mechanism at a molecular level was suggested, based on the ATR-FTIR investigations combined with the mass spectroscopy (MS) analysis. Different from those observed in other semiconductor photocatalysts, a direct hydroxyl radical formation mechanism was suggested, where two adsorbed OH radicals became adsorbed H_2O_2 or adsorbed O_2^{2-}, which caused the O_2 evolution with two other holes [38].

On different α-Ga_2O_3 surfaces, namely (001), (100), (110), and (012), water adsorption and activation were explored by means of DFT calculations. The dissociative water adsorption on all the studied low-index surfaces is thermodynamically favorable, and the most preferentially exposed surface is (012). The computation for the electrochemical model was used to investigate both the HER and the OER on α-Ga_2O_3 surfaces. The results indicate that the (100) and (110) surfaces are the most favorable ones for HER and OER, respectively, but they have low stability [39].

5. IrO_2 and RuO_2

Iridium oxide (IrOx) was used as the OER co-catalyst of the $Y_2Ti_2O_5S_2$ photocatalyst for visible light water splitting [40]. Ir-based catalysts are the catalysts of choice to date; nevertheless, their high price and scarcity have greatly hampered the widespread utilization of the PEM water electrolysis technique [41]. On the other hand, ruthenium (Ru), at higher earth abundance and lower price, possesses superior catalytic activity to Ir. However, Ru is prone to dissolution and results in low stability that cannot be applied in practical devices [41]. The surface stability and dissolution of three prominent electro(photo)catalysts for water splitting: RuO_2, IrO_2, and TiO_2 in the rutile phase was investigated by using a combination of ab initio steered molecular dynamics, enhanced sampling, and ab initio thermodynamics. A distinct site-specificity in the dissolution of the RuO_2(110) surface was identified, whereas no such surface site exists for the IrO_2(110) surface [42]. However, the mechanistic interplay between the OER and material degradation during water electrolysis is not yet well understood even for the most studied OER electrocatalysts such as IrO_2 and RuO_2 [43].

Anodically grown IrO_X catalyst films were studied using Raman spectroscopy. In addition to deuteration and ^{18}O substitution experiments, theoretical models were also constructed using DFT to interpret the experimental data. The material was found to be composed of $[IrO_6]_n$ edge-sharing polyhedra (with $n \geq 3$) and characterized over a large potential range (0.0–1.8 V). Ir centers are connected to each other via μ-O type oxygen linkages that allow for the Ir centers to electronically couple to each other. Oxidation of Ir^{3+} to Ir^{4+} at 0.7–1.2 V within a μ-O linked polymeric geometry resulted in a blue coloration of the material at high potentials. Theoretical calculations indicated that the optical transition responsible for the color is essentially an Ir-to-Ir charge transfer transition [44].

For a catalyst system of Ir oxide nanocluster, a surface hydroperoxide, Ir-OOH, as an intermediate of OER has been detected by recording the FTIR spectra of the OO vibrational mode at 830 cm^{-1}. The detection was achieved upon oxidation of water under pulsed excitation of a visible light sensitizer $[Ru(bpy)_3]^{2+}$ [45]. The OER mechanism of IrOx was investigated based on charge accumulation, where the valence change in Ir is more favorable than O–O bond formation. In situ evanescent wave spectroscopy revealed that an intermediate assignable to Ir^{5+} with oxygen ligands in opposite spin served as the precursor of OER regardless of pHs (2 to 12), as the generation of this species was not related to valence changes in Ir. The results confirmed that charge accumulation was not rate-limiting for OER on IrO_X, which is a key mechanistic difference between IrOx and less efficient 3d metal electrocatalysts [46]. Time-resolved operando spectroelectrochemistry was employed to investigate the redox-state kinetics of IrO_X electrocatalyst films for both water and hydrogen peroxide oxidation. Three different redox species involving Ir^{3+}, Ir^{3x+}, Ir^{4+}, and Ir^{4y+} were identified spectroscopically. A first-order reaction mechanism was suggested for H_2O_2 oxidation driven by Ir^{4+} states, and a higher-order reaction mechanism involving the cooperative interaction of multiple Ir^{4y+} states for water oxidation [47].

On calcined and uncalcined IrO_2, operando XAS spectroscopy was utilized to study the OER under different protocols. At the elevated OER potentials above 1.5 V, stronger Ir−Ir interactions were observed, which were more dominant in the calcined [48].

With first-principle calculations integrated with implicit solvation at constant potentials, the detailed atomistic reaction mechanism of OER was examined for the IrO_2(110) surface. The surface phase diagram was determined, and the possible reaction pathways including kinetic barriers, and computed reaction rates were explored based on the microkinetic models [49]. The classical mechanism at the IrO_2(110) surface was reconsidered. The OER follows a bi-nuclear mechanism with adjacent top surface oxygen atoms as fixed adsorption sites, whereas the Ir atoms underneath play an indirect role and maintain their saturated six-fold oxygen coordination at all stages of the reaction. The oxygen molecule is formed, via an Ir–OOOO–Ir transition state, by association of the outer oxygen atoms of two adjacent Ir–OO surface entities, leaving two intact Ir–O entities at the surface behind [50].

An IrO_2 nanoribbon of monoclinic phase, which is distinct from tetragonal rutile IrO_2, was provided by a molten alkali mechanochemical method. The intrinsic catalytic activity of IrO_2 nanoribbon was higher than that of rutile IrO_2 due to the low d band center of Ir in this special monoclinic phase structure as confirmed by DFT calculations [51]. Ultrasmall Pd@Ir core–shell nanoparticles (5 nm) with three atomic layers of iron–carbon nanotubes were constructed as an exceptional bifunctional electrocatalyst in acidic water splitting. Due to the core–shell structure, strain generated at heterointerfaces leads to an up-shifted d band center of Ir atoms contributing to a 62-fold better mass activity than commercial IrO_2. Moreover, electronic hybridization suppresses the electrochemical dissolution of Ir, resulting in the achievement of robust stability [52].

$Ir_XRu_{1−x}O_2$ (x = 1, 0.6, 0.3, and 0) was prepared by the hydrolysis synthesis, and a mechanistic study of the OER was reported. The polarization curves recorded at pHs of 0 to 3 could be well-fitted to a model consisting of a series of concerted electron–proton transfer reactions (a mononuclear mechanism). It was suggested that the third or fourth step is rate-determining for RuO_2 and IrO_2, respectively [53].

For single-crystal RuO_2(110) in acidic electrolytes, the surface structural changes as a function of potential were investigated by in situ surface X-ray scattering measurements with DFT calculations. The redox peaks at 0.7, 1.1, and 1.4 V vs. RHE could be attributed to the surface transitions associated with the successive deprotonation of $*H_2O$ on the coordinately unsaturated Ru sites and hydrogen adsorbed to the bridging oxygen sites. At potentials relevant to the OER, an *OO species on the unsaturated Ru sites was detected, which was stabilized by a neighboring *OH group on the unsaturated Ru site or bridge site. A new OER pathway, where the deprotonation of the *OH group is used to stabilize *OO, was found to be rate-limiting [54]. For the RuO_2(110) surface, the DFT method considering a possible magnetic effect on the electronic configuration was applied to calculate the thermodynamic stability of possible O versus OH terminations and their effect on the free energies of the OER steps. The magnetic moment of RuO_2 supplies an important contribution to obtaining a low overpotential and to its insensitivity to the exact O versus OH coverage of RuO_2(110) surface [55].

The OER kinetics on RuO_2 rutile (110), (100), (101), and (111) orientations were experimentally investigated, finding (100) the most active. The potential involvement of lattice oxygen in the OER mechanism was assessed with online electrochemical mass spectrometry. No evidence of oxygen exchange on these oriented facets in acidic or basic electrolytes suggested that lattice oxygen is not exchanged in catalyzing OER on crystalline RuO_2 surfaces [56].

Rh doping for RuO_2 and surface oxygen vacancies to precisely regulate unconventional OER reaction paths via the Ru–O–Rh active sites have been reported. Quasi in situ/operando characterizations demonstrated the recurrence of reversible oxygen species under working potentials for enhanced activity and durability. It was theoretically revealed that Rh-RuO_2 passes through a reaction path of lattice oxygen-mediated mechanism, which is more optimal than the oxygen vacancy site mechanism. The synergistic interaction of defects and Ru–O–Rh active sites causes the *O formation with the rate-determining step, breaking the barrier limitation (*OOH) suggested by the traditional AEM process [57].

6. Perovskite as Electrocatalysts

Perovskite-type oxide nanocrystals (AxByOz), which possess distinct thermal stability, ionic conductivity, and electron mobility properties, have attracted increasing interest as efficient OER catalysts [58]. The electronic structure of perovskite-type nanocrystals plays a decisive role in electrocatalytic performance, the orbital filling, metal–oxygen hybridization, and electron correlations of perovskite-type oxide nanocrystals for high-performance OER catalysis were systematically investigated [58]. By using soft X-ray emission and absorption spectroscopies, perovskite OER catalysts were analyzed for the partial density of states on an absolute energy scale. Decreasing the solid-state charge-transfer energy of perovskite can change the mechanisms of the OER from electron-transfer-limited to proton–electron-coupled, and to proton-transfer-limited reactions [59]. The perovskite electrocatalysts with noble metals exhibited the smallest overpotential in various types of catalysts as shown in **Figure 6** [60].

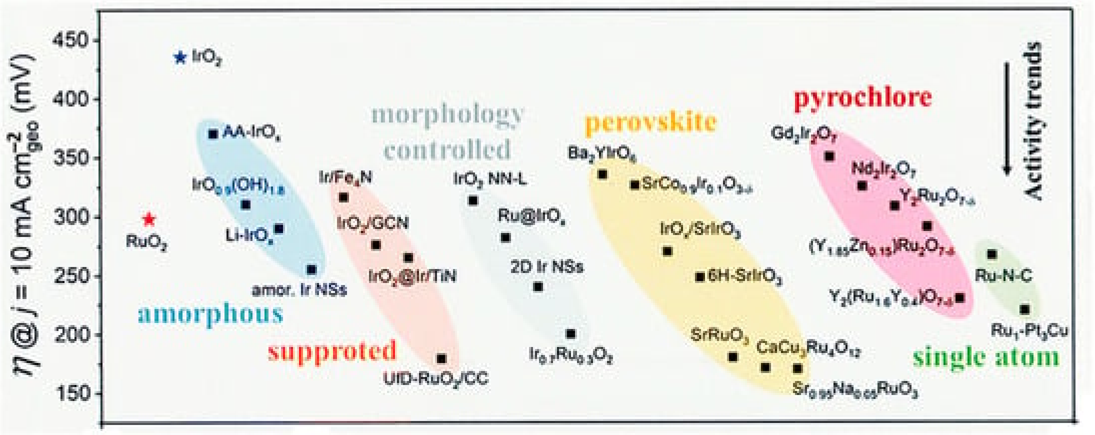

Figure 6. Electrocatalytic OER activities (overpotential at j = 10mA cm^{-2})) on noble metal (Ir, Ru, Pt) based catalysts under acidic conditions. Reproduced from *Nanoscale* **2020** **[60]** with permission from the Royal Society of Chemistry.

On various $La_XSr_{1-x}CoO_3^{-\delta}$ as OER catalysts, a general strategy was demonstrated for steering the two mechanisms, AEM and LOM. By delicately controlling the oxygen defect contents, the dominant OER mechanism can be arbitrarily transformed between AEM-LOM-AEM accompanied by a volcano-type activity variation trend. Experimental and computational evidence explicitly revealed that the phenomenon is due to the fact that the increased oxygen defects alter the lattice oxygen activity with a volcano-type trend and preserve the Co^0 state for preferably the OER [61].

For $NdNiO_3$, the link between structural anisotropy and the OER catalytic activity was established by DFT calculation. The $NdNiO_3$ with (100), (110), and (111) orientations display similar oxidative states and metal–oxygen covalence characteristics, but distinct OER activities in experimental results were in the order of (100) > (110) > (111). DFT results confirm that film orientation is a critical determinant of the reaction mechanism. The OER on the (100)-surface favors proceeding via a LOM. In contrast, the reaction on (110)- and (111)-surfaces followed the AEM. The anisotropic oxygen vacancy formation energy and stability are strongly correlated to the reaction mechanism and performance [62]. On $LaNiO_3$ epitaxial thin films, electrochemical scanning tunneling microscopy (EC-STM) was used to directly observe structural dynamics during the OER. Based on the comparison of dynamic topographical changes in different compositions, reconstruction of surface morphology originating from the transition of the Ni species on the surface termination during the OER was proposed [63]. The change in surface topography was induced by $Ni(OH)_2$/NiOOH redox transformation by quantifying STM images [63].

On $La_{1-x}NiO_3$ perovskite electrocatalysts, direct O–O coupling promoted the OER activity at the interfacial active sites for decorated Ag nanoparticles. The theoretical calculation revealed that oxygen evolution via the dual-site mechanism with direct O–O coupling becomes more favorable than that via the conventional AEM. At x = 0.05, the electrocatalyst showed 20 times higher mass activity than that of the IrO_2 electrocatalyst, and the activity increased to 74 times after an accelerated durability test [64].

$Ca_{2-x}IrO_4$ nanocrystals exhibited a very high stability of about 62 times that of benchmark IrO_2. Lattice resolution images and surface-sensitive spectroscopies demonstrated the Ir-rich surface layer with high relative content of Ir^{5+} sites, which is responsible for the high activity and long-term stability. Combining operando IR spectroscopy with the XAS method, key intermediates of $Ir^{6+} = O$ and $Ir^{6+}OO^-$ on Ir-based oxides electrocatalysts were observed, and they were stable even just from 1.3 V vs. RHE. DFT calculations indicated that the catalytic activity of Ca_2IrO_4 is enhanced remarkably after leaching the surface Ca ions because Ir = O and $IrOO^-$ intermediates can be stabilized on positively charged active sites of the Ir-rich surface layer [65]. Layered perovskite Sr_2IrO_4 was chemically exfoliated into protonated colloidal nanosheets with an undamaged perovskite framework. This OER catalyst exhibited about 10 times higher activity than the IrO_2 catalyst film. As shown in **Figure 7**, DFT calculation indicated that electrons from the inner Ir atom to the surface were observed in IrO_2 (e) but not in the case of perovskite nanosheet (d), then the free energy of O* is moderate as shown in (a) compared with the case of IrO_2

(b). Thus, the structural hydroxyl groups on the surface of protonated nanosheets participate in the catalytic cycle [66].

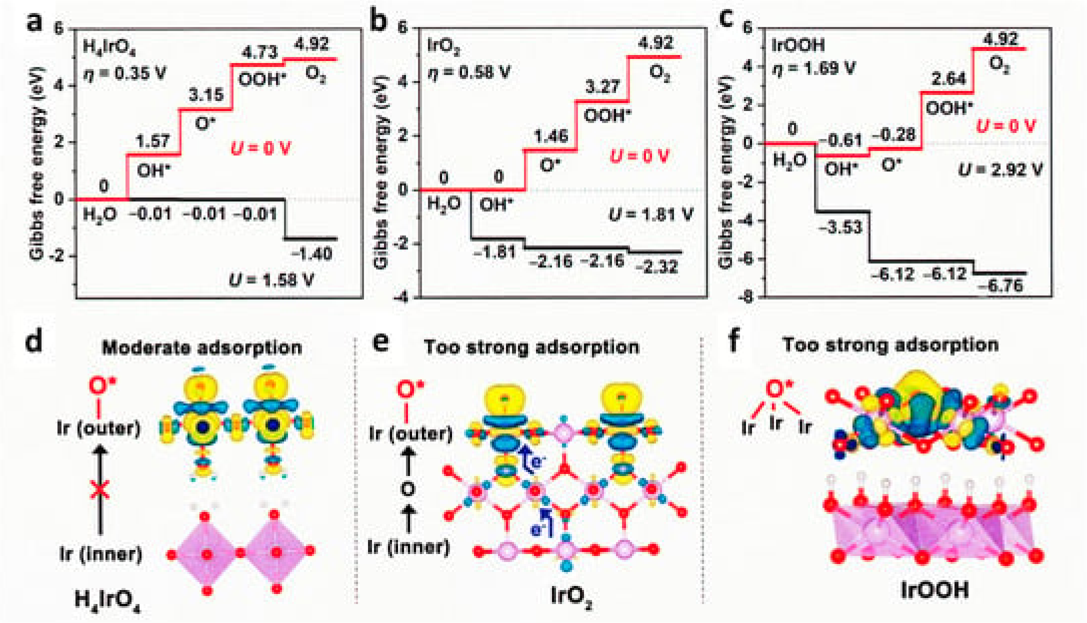

Figure 7. DFT calculation of HION, IrO_2, and IrOOH. (**a**–**c**) Gibbs free energy diagrams of H_4IrO_4, IrO_2, and IrOOH for OER at Ir sites. (**d**–**f**) Charge density difference induced by oxygen adsorption of H_4IrO_4, IrO_2, and IrOOH at Ir sites. Reproduced from *ACS Catal*. **2022** [66] with permission from the American Chemical Society.

7. Transition Metal (TM) Compounds

Multicomponent transition metal oxides and (oxy)hydroxides are the most promising OER catalysts due to their low cost, adjustable structure, high electrocatalytic activity, and outstanding durability. Co-, Ni-, and Fe-based OER catalysts have been considered to be potential candidates to replace noble metals, especially for electrocatalysts, due to their tunable 3d electron configuration and spin state, versatility in terms of crystal and electronic structures, as well as abundance in nature [67]. The latest advances in the rational design of the related OER electrocatalysts and the modulation of the electronic structure of active sites were comprehensively summarized, besides a brief overview of the mechanisms of OER and the theory and calculation criteria [68].

Wang et al. reviewed the fundamental understanding of the electronic structure of low-cost TM oxide-based catalysts for electrochemical OER, and its relationship with the catalytic activity and the reaction mechanism was discussed [69]. Feng et al. reviewed the relationship between TMs and OER catalyst activity, and then the mechanism of synthesis strategy in different types of TMs-based catalysts was summarized [70]. Guo et al. reviewed the state-of-the-art amorphous transition metal-based OER electrocatalysts, involving oxides, hydroxides, sulfides, phosphides, borides, and their composites, and then the practical application and theoretical modeling of the OER mechanisms in the OER were presented [71]. Though transition metal phosphides often exhibit excellent HER activity, the OER catalytic performance is not outstanding. Huang et al. reviewed the strategies for preparing highly active OER catalysts of transition metal phosphides [72].

The early transition metals (Ti, V, and Cr) can form very stable M=O units, while the late transition metals (Ni and Cu) can only theoretically form unstable M=O structures. On the other hand, for Mn, Fe, and Co, the metal-oxo motif switches between two valence tautomers in the form of $Mn^{+1} = O^{2-}$ and $Mn–O•^{-}$. The former with an electrophilic oxygen atom can proceed via the acid–base WNA pathway to form the O–O bond, whereas the latter favors the oxygen radical coupling pathway for O–O bond formation [73].

7.1. CoOx

CoOOH was selected as the OER co-catalyst of aluminum-doped strontium titanate (SrTiO:Al) photocatalyst to attain almost unity in the internal quantum efficiency of UV-induced water splitting with Rh/Cr HER co-catalyst [74]. The recent progress of Co_3O_4-based electrocatalytic materials for the acidic OER was presented with particular reference to the catalytic mechanism and guidelines for the design principles from both experimental and theoretical perspectives [75]. Afterward, emerging strategies were outlined to improve the catalytic performance of Co_3O_4-based acidic OER catalysts, including phase engineering, component regulation with doping, composite with carbon-based materials, and multi-phase hybridization [75].

For the application of Co oxides to photocatalysts, operando XPS measurements were performed. The catalyst undergoes chemical–structural transformations as a function of the applied anodic potential, with complete conversion of the $Co(OH)_2$ and partial conversion of the spinel Co_3O_4 phases to cobalt oxyhydroxide, CoO(OH), under precatalytic electrochemical conditions. This interpretation revealed that the presence of $Co(OH)_2$ enhances catalytic activity by promoting transformations to CoO(OH) [76]. To study the mechanism of OER on CoO(OH), operando X-ray absorption and Raman spectroscopy revealed that a Co(IV) species, CoO_2, is the dominating resting state of the catalyst. Oxygen isotope exchange experiments showed that a cobalt superoxide species is an active intermediate in the OER. This intermediate is formed concurrently with the oxidation of CoO(OH) to CoO_2. Combining spectroscopic and electrokinetic data, the rate-determining step of the OER was identified as the release of dioxygen from the superoxide intermediate [77].

By using a water-in-salt electrolyte, the water activity was systematically tuned and the mechanism as a function of applied potentials in water electrolysis was probed. The mechanism is sensitive to the applied potential. The Co-OO-Co bond forms via an intramolecular oxygen coupling mechanism at low potentials, whereas it proceeds through a WNA mechanism by forming Co-OOH at high potentials [78].

The morphology-dependent analysis for well-defined crystalline CoO(OH) revealed that the active sites are exclusively located at lateral facets rather than basal facets. Theoretical calculations show that the coordinately unsaturated Co sites of lateral facets upshift the O 2p-band center closer to the Fermi level, thereby enhancing the covalency of Co-O bonds to yield the reactivity [79]. The sequential oxidation kinetics with Co_3O_4 nanoparticles involving multi-active sites for water oxidation in the OER catalytic cycle were resolved by applying quasi-operando transient absorption spectroscopy to a typical photosensitization with Ru-dye and sacrificial electron donor. The Co^{IV} intermediate distribution plays a determining role in OER activity and results in the slow overall OER kinetics [80]. The redox process between Co^{III} and Co^{IV} species does not follow a proton-coupled electron transfer mechanism that is thought to be common prior to the OER, but it involves a proton-decoupled electron transfer, clarified by isotope labeling experiments and in situ electrostatic modulation [81].

An oxygen vacancy (Vo)-rich environment facilitates the reconstruction of Co_3O_4 to the $Co(OH)_2$ intermediate with proton vacancies ($Co^{II}O_{x(}OH)_y$), which is favorable for the formation of the active species of CoO(OH). Correlative operando Raman spectra characterizations and electrokinetic analyses indicated that a moderate Vo density can switch the O–O bond formation pathway, from a WNA to an INA pathway, which is more kinetically favorable for water oxidation [82]. As shown in **Figure 8**b with O vacancy, at step 3, three protons and one electron are removed to form Co-O(OH). At step 4, Co^{III} sites of Co-O(OH) are oxidized to Co^{IV} which can be deprotonated (step 8) by hole attack oxo ligand Co^{IV} = O forms a Co-O-O triangle (step 9), and then becomes Co^{II}-OO• (step 10). At the next oxidation (step 10), O_2 is released and Co^{II} back to Co^{III} with the coordination of water. The I2M process was excluded based on the experimental results of using the $H_2{}^{18}O$ isotope [82].

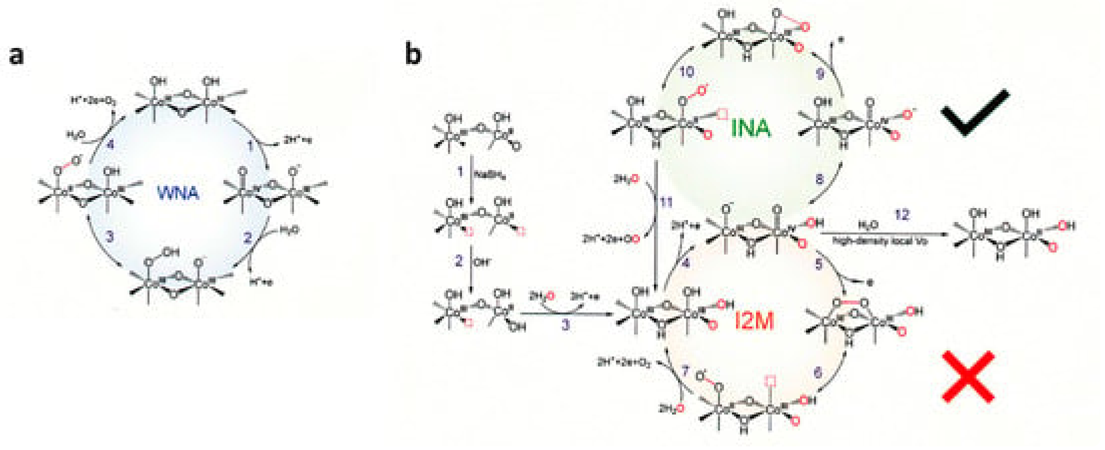

Figure 8. Proposed reaction mechanisms of the OER for (**a**) Co_3O_4 and (**b**) Vo-Co_3O_4. Oxygen vacancy (Vo) prepared by $NaBH_4$ reduction was represented by the red dotted boxes. WNA = water nucleophilic attack, INA = intramolecular nucleophilic attack, and I2M = interaction between the two metal-O units. Reproduced from *ACS Catal.* **2023** [82] with permission from the American Chemical Society.

Amorphous CoO(OH) layer architecture was loaded onto the surface of TiO_2. Tafel analysis, EIS, and CV methods showed that the carrier transfer barrier within the electrode and the transition of $Co^{III}O(OH)$ to $Co^{IV}O(OH)$ have the dominating effects on the photoelectrochemical performance. Theoretical calculation revealed that the interface between the CoO(OH) and TiO_2 improves the electronic transfer ability among Co sites [83]. Amorphous CoO(OH) layers are electrochemically synthesized on the surface of various cobalt sulfides CoS_α and found to decrease the intermolecular energy gap. The decrease in the energy gap accelerates the formation of OER-active high-valent Co^{IV} species [84].

7.2. NiOx

For the nascent ultra-small nickel oxyhydroxide (NiOOH) particles (<3 nm), the thermodynamics of Ni dissolution was calculated by using first-principles theory at a near-neutral pH range, and the mechanism of OER on the γ-

NiOOH surface was clarified. It was concluded that (i) ∼4% Ni cations on the surface of γ-NiOOH dissolve at pH = 7 and 1.73 V vs. RHE; (ii) on the pristine γ-NiOOH surface, OER proceeds via the “lattice peroxide” mechanism ($^*H_2O \rightarrow {}^*OH \rightarrow {}^*O{-}O_{latt}H^* \rightarrow O{-}O_{latt} \rightarrow O_2$) with an overpotential of 0.70 V; (iii) in the presence of Ni cationic vacancies, OER proceeds via the “hydroperoxide” mechanism ($^*OH + {}^*H_2O \rightarrow {}^*2OH \rightarrow {}^*OOH \rightarrow O_2$) with an overpotential of 0.40 V [85].

For NiOOH-based materials, light-triggered reversible geometric conversion between octahedron (NiO_6) and square planar (NiO_4) was proposed. The unit cell was undergone to achieve electronic states with alternative metal and oxygen characters throughout the oxygen evolution process. Utilizing this electron transfer pathway can bypass the potential limiting steps, that is, O–O bonding in the AEM and deprotonation in the LOM. As a result, the electrocatalysts that operate through this route showed superior activity compared with previously reported electrocatalysts [86][87].

By incorporating Fe and V into $Ni(OH)_2$ lattices, OER activity was improved. X-ray photoelectron/absorption spectroscopies revealed the synergistic interaction between Fe/V dopants and Ni in the host matrix, which subtly modulates local coordination environments and electronic structures of the Fe/V/Ni cations. Further, in situ XAS analyses manifested contraction of metal–oxygen bond lengths in the activated catalyst, with a short V–O bond distance. DFT calculations indicated that the V site of the Fe/V co-doped NiOOH gave near-optimal binding energies of OER intermediates and had lower overpotential compared with Ni and Fe sites [88]. A series of Mn-, Co-, Fe-, and Zn-doped nickel oxides were investigated by using operando UV−vis spectroscopy coupled with time-resolved stepped potential spectroelectrochemistry. The Ni^{2+}/Ni^{3+} redox peak potential was found to shift anodically from Mn- < Co- < Fe- < Zn-doped samples, suggesting a decrease in oxygen binding energetics from Mn- to Zn-doped samples. The OER kinetics had a second-order dependence on the density of these oxidized species, suggesting a chemical rate-determining step involving the coupling of two oxo species. The intrinsic turnover frequency per oxidized species exhibits a volcano trend with the binding energy of oxygen on the Ni site, having a maximum activity for the Fe-doped sample as shown in **Figure 9**. For Ni centers that bind oxygen too strongly (Mn- and Co-doped oxides), OER kinetics is limited by O–O coupling and oxygen desorption, while for Ni centers that bind oxygen too weakly (Zn-doped oxides), OER kinetics is limited by the formation of oxo groups [89].

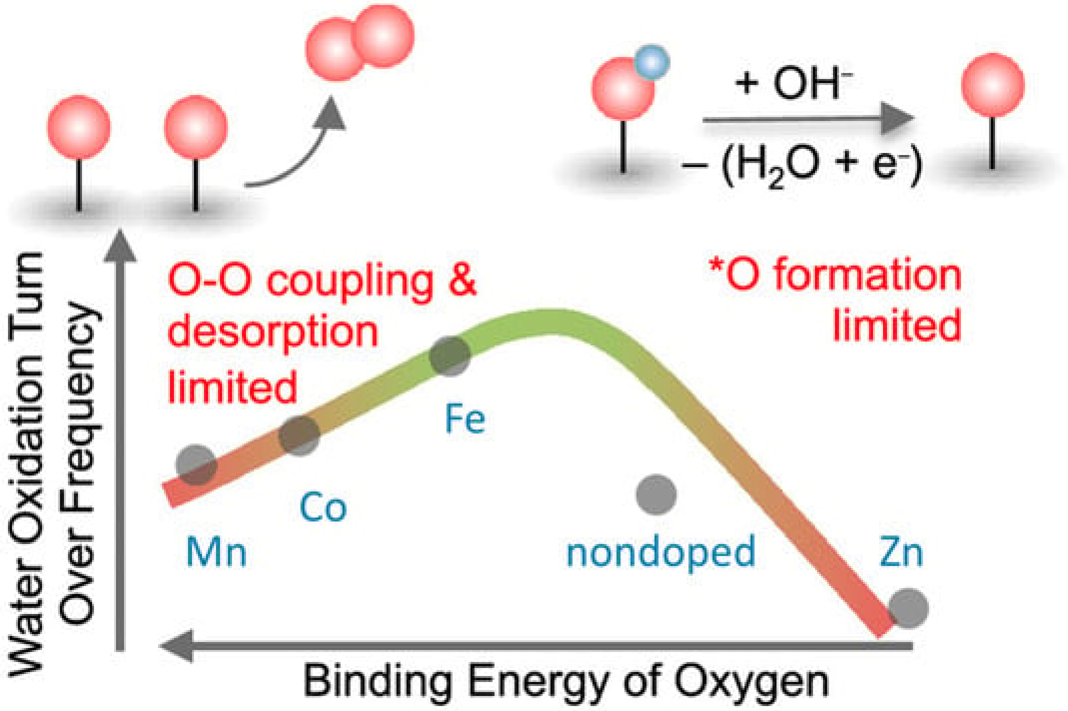

Figure 9. Decrease in the binding energy from Zn- to Mn-doped nickel oxides showed a volcano-type OER activity by changing the rate-determining step from •O formation to O-O coupling. Reproduced from *J. Am. Chem. Soc.* **2022** [89] with permission from the American Chemical Society.

Oxygen vacancy-enriched porous NiO/In_2O_3 nanofibers (Vo–NiO/In_2O_3@NFs) were fabricated for efficient OER electrocatalysis. Abundant Vo modulated the electronic configuration of the catalyst for altering the adsorption of intermediates to reduce the OER overpotential and promote *O formation, upshifting the d band center of metal centers near the Fermi level, and also increasing the electrical conductivity and enhancing the OER reaction kinetics simultaneously. In situ Raman spectra suggested that the Vo can render the NiO/In_2O_3 more easily reconstructible on the surface during the OER course [90].

DFT +U calculations revealed that Ir-doping of a β-NiOOH(001) surface enhanced the electric conductivity while also activating an oxygen site involving three Ni atoms to realize a remarkably low OER overpotential of only $\eta = 0.46$ V, much lower than the oxygen site involving three Ni atoms in pristine β-NiOOH ($\eta = 0.66$ V) [91]. Since theoretical calculations predicted that Co, Rh, and Ir dopants would lead to low overpotentials to improve the OER activity of Ni-based hydroxides, an experimental confirmation on the altered OER activities for a series of metals (Mo, W, Fe, Ru, Co, Rh, Ir) doped into γ-NiOOH has been reported [92]. The in situ electrical conductivity for metal-doped γ-NiOOH correlated well with the trend in enhanced OER activities. The DFT calculations, which suggested that the intrinsic connections to the double exchange interaction between adjacent metal ions with various d orbital occupancies, rationalized the experimental results, serving as an indicator for the key metal-oxo radical character [92].

7.3. FeOx

Recent advancement and progress in initializing Fe-based OER electrocatalysts with different supporting materials, including carbon-based materials, layered double hydroxides, Prussian blue analogous, metal–organic frameworks, were reviewed by Xiong et al. [93]. In the review, the OER mechanism and some typical OER electrochemical parameters of Fe-based electrocatalysts supported on various supporting materials from experimental and theoretical viewpoints were highlighted. Some challenges and expectations for promoting the catalytic performance were described [93].

In photoelectrochemical (PEC) water oxidation on hematite (α-Fe_2O_3), the mechanism of the subsequent rate-limiting O–O bond formation step was investigated by rate law analysis based on EIS measurements and probing the reaction intermediates with operando FTIR spectroscopy. Distinct reaction orders of ~1 and ~2 were observed in near-neutral and highly alkaline environments, respectively. The unity rate law in near-neutral pH regions suggests a mechanism of WNA to –Fe=O to form the O–O bond. Operando observation of a surface superoxide species by FTIR further confirmed this pathway. In highly alkaline regions, coupling of adjacent surface trapped holes (I2M) becomes the dominant mechanism. While both are operable at intermediate pHs, the mechanism switch from I2M to WNA induced by local pH decrease was observed at a high photocurrent level as shown in **Figure 10** [94]. In the recent report, transient photocurrent measurements for hematite photoanodes revealed that the OER rate has a third-order dependence on the surface hole density. A mechanism wherein the reaction proceeds by accumulating oxidizing equivalents through a sequence of one-electron oxidations of surface hydroxy groups was proposed. The key O–O bond formation step occurs by the dissociative chemisorption of a hydroxide ion involving three oxyl sites [95].

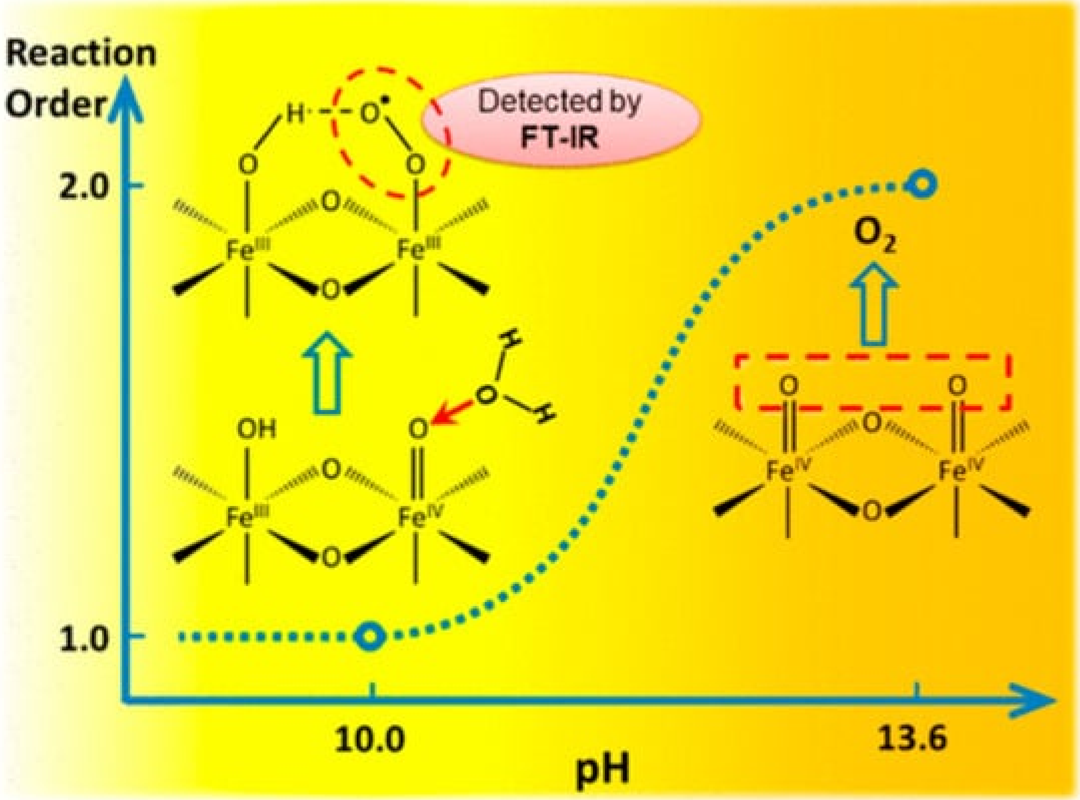

Figure 10. In photoelectrochemical water oxidation on α-Fe_2O_3, the OER mechanism switches from WNA to I2M at a strong alkaline solution. Reproduced from *J. Am. Chem. Soc.* **2018** [94] with permission from the American Chemical Society.

Polycrystalline γ-FeO(OH), synthesized at room temperature, was used as a stable, although reactive, anode for OER, and electrokinetic studies were performed to unravel the OER pathway [96]. The cell temperature, hydroxyl ion concentration, and the cation of the supporting electrolyte were varied, and the influence of external bias on the OER activity was recorded. Tafel slope and charge-transfer resistance values at high temperatures up to 65 °C unambiguously highlight the influence of the thermodynamic barrier and electron transfer kinetics. The faster OER kinetics on polycrystalline γ-FeO(OH) can also be attributed to an appreciably low activation energy, where the variation of the electrolyte concentration indicated a first-order dependence on the OH^- concentration. The deuterium isotope effect implicated the dissociation of hydroxyl ions on the polycrystalline γ-FeO(OH) as the rate-determining step. The direct effect of cations such as Li, Na, and K of the electrolyte on OER indicated a weak interaction of the cations with the surface-active [Fe^{III}-OH] species [96].

Fe_3O_4 with oxygen vacancies (Fe_3O_4-V_O) was synthesized via the Ar ion irradiation method and its OER activity was greatly improved by properly modulating the electron density around Fe atoms, which were evaluated with XANES and EXAFS methods. DFT results indicated the enhancement in desorption of the *OOH groups, which significantly reduced the OER reaction barrier. Actually, the Fe_3O_4-Vo catalyst showed a better overpotential than commercial RuO_2 [97].

Ni-, Co-, and Yb-doped FeO(OH) nanorod arrays grown directly on carbon cloth (CC) are synthesized by a simple one-step hydrothermal method. The doped Ni^{2+} and Co^{2+} can occupy Fe^{2+} and Fe^{3+} sites in FeO(OH), increasing the concentration of oxygen vacancies and the doped Yb^{3+} with a larger ionic radius can occupy the interstitial sites, which leads to more edge dislocations. The oxygen vacancies and edge dislocations greatly enrich the active sites in FeO(OH)/CC. In addition, DFT calculations confirmed that doping Ni^{2+}, $Co^{2+,}$ and Yb^{3+} modulates the electronic structure of the main active Fe sites, bringing its d-band center closer to the Fermi level and reducing the Gibbs free energy change in the rate-determining step of the OER [98].

7.4. MnOx

Nature uses a Mn cluster for water oxidation in PS II, and thus, water oxidation using Mn clusters is interesting in artificial water-splitting systems. An ultra-thin manganese oxide (MnO_X) was selected as a co-catalyst to modify the surface of $BiVO_4$ photoanode by a spray pyrolysis method [99]. The PEC measurements demonstrated that the surface charge transport efficiency strikingly increased by the MnO_X modification. After applying Ar plasma to the $BiVO_4$/MnOx sample, the transport efficiency further increased, and it was around 7 times higher compared with that of pristine $BiVO_4$ samples. The remarkable PEC performance could be attributed to the increased charge carrier density, extended carrier lifetime, and additional exposed Mn active sites on the $BiVO_4$ surface [99].

An α-Mn_2O_3/FTO electrocatalyst was used in nonaqueous (CH_3CN and DMF) and aqueous 0.1 M KPi (pH 7.0) solutions for kinetic studies of heterogeneous water oxidation. The rate of water oxidation was first order in catalyst concentration and in H_2O concentration. The square wave and cyclic voltammetry measurements revealed the stepwise proton-coupled electron transfer oxidations of the active $Mn^{II}–OH_2$ site to $Mn^{III}–OH$ and then to $Mn^{IV}=O$ and finally an electron transfer oxidation of $Mn^{IV}=O$ to $Mn^{V}=O$ species. The $Mn^{V}=O$ species undergoes a rate-limiting O atom transfer to H_2O to give a $Mn^{III}–OOH_2$ species that, in turn, undergoes further oxidations to release O_2 [100].

An Mn–K cluster was investigated for electrochemical water oxidation. By using XAS, SEM, TEM, XRD, FTIR spectroscopy, and electrochemical methods, it was revealed that conversion into nanosized Mn oxides occurred for the cluster, and the nanosized Mn oxides are the true catalyst for water oxidation [101].

The Mn_3O_4 nanocatalyst, which exhibits superb catalytic activity for water oxidation under neutral conditions, was analyzed for the complex capacitance. By the change in Mn valence between Mn^{II} and Mn^{IV}, the charge was accumulated on the catalyst surface prior to the rate-determining O–O bond-forming step. The dissipation ratio was proposed for understanding the energy balance between charge accumulation and charge consumption for chemical O–O bond formation [102]. In Mn_3O_4 nanoparticles, a profile imaging technique was exploited to understand the correlation between surface atomic structures and the OER. The surface structures of Mn_3O_4 nanoparticles were changed by the reaction and the surface Mn ions were reconstructed. The commonly considered active sites disappeared from the reconstructed planes, whereas Mn ions were still exposed at the edges of nanoparticles. Thus, the surface reconstructions can deactivate low-index surfaces of Mn oxides in the OER process, which was further validated by DFT calculations [103].

An $Mn^{VII}=O$ intermediate during electrocatalytic water oxidation by a c-disordered δ-MnOx was identified as an onset-potential-dependent reduction peak at 0.93 V. This intermediate is proven to be highly reactive and much more oxidative than permanganate ion. Thus, a new catalytic mechanism for water oxidation catalyzed by Mn oxides was proposed with the involvement of the $Mn^{VII}=O$ intermediate in a resting state and the Mn^{IV}-O-$Mn^{VII}=O$ as a real active species for O-O bond formation. **Figure 11** shows the proposed catalytic cycle, involving $Mn^{VII}=O$, in the MnOx-catalyzed water-oxidation reaction. The overall mechanistic process involves charge accumulation (S_0/S_3), charge rearrangement (S_3/S_4), active-state formation ($S_4/S_{4'}$), and oxygen evolution ($S_{4'}/S_0$) [104].

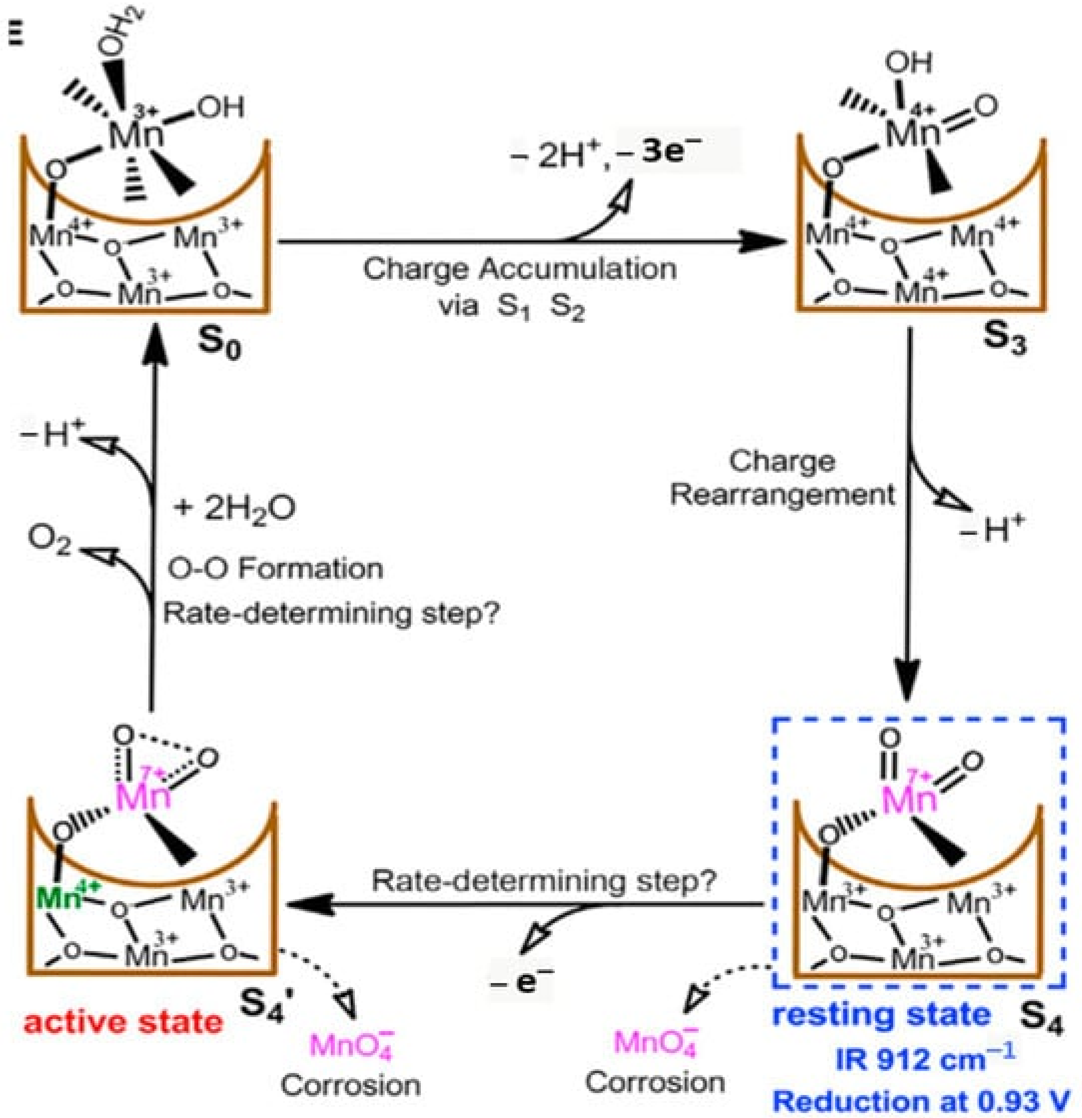

Figure 11. Proposed mechanism in MnO_x-catalyzed OER. Reproduced from *iScience* **2018** [104] under the license of CC BY 4.0 of Elsevier.

7.5. Mixed Metal Oxides

Two or three transition metals are mixed to form oxides of high electrocatalytic performance for water electrolyzers at a low cost. An NiFe oxide catalyst was employed as the anode catalyst with an NiMo oxide cathode catalyst with a high-performance perovskite-Si tandem solar cell, achieving a record 20% STH efficiency [105]. Nickel ferrite, $NiFe_2O_4$, cobalt ferrite, and $CoFe_2O_4$, are efficient and promising anode catalyst materials in the field of electrochemical water splitting.

In Ni-Fe water oxidation electrocatalysts, Ni is likely not an active site for water oxidation, because Ni cannot achieve high-oxide states in aqueous environments at relevant potentials [106]. For the OER of $NiFeO_xH_y$, the addition of Co^{2+} cation increased the current density by 32.7% by the cation transport effect [107]. Using operando XAS, it was revealed that Ni oxidizes from the initial +2 oxidation state to the +3/+4 state [108]. For Ni-Fe oxyhydroxides, in situ monitoring of the Fe active site number and turn-frequency number provided important insights into the activity degradation/regeneration caused by Fe dissolution/adsorption as well as site-dependent activity and stability [109]. In the case of $NiFe_2O_4$, an Fe-site-assisted LOM pathway as the preferred OER mechanism was predicted. On the other hand, in the case of $CoFe_2O_4$, an Fe-site-assisted LOM pathway and a Co-site-assisted AEM pathway could both play a role [110].

Amorphous/crystalline $NiFe_2O_4$ induced by vanadium doping showed a superior electrocatalyst and long-term stability [111]. For amorphous Ni-Fe mixed metal oxides, analysis of the XAS revealed local structural transitions. A dual-site OER reaction mechanism was proposed, in which potential and rate-determining steps occur at Ni and Fe sites, respectively [112].

An Fe/Ca-based bimetallic oxide, $CaFe_2O_4$, exhibited outstanding OER activity in alkaline media. DFT calculations suggested an unconventional mechanism via the direct formation of O–O bonds between two oxygen intermediates, which are adsorbed on a multi-iron site on the catalyst surface [113].

On spinel $NiCo_2O_4$ abundant Co defects were preferentially produced by tuning the M–O bond length. Theoretical calculations and experiments proved that Al doping elongated the Co–O bond and promoted the ionization of Co under plasma treatment [114]. Spinel Co_2MnO_4 showed higher OER activity, most probably due to the ideal binding energies of the OER intermediates [115].

For modulated NiFeX and FeCoX (X = W, Mo, Nb, Ta, Re, and MoW) oxyhydroxide catalysts, in situ and ex situ soft and hard XAS were used to characterize the oxidation transition and facilitate the lower OER overpotential [116]. (Co–Fe–Pb)Ox in acidic solutions through a cobalt-selective self-healing mechanism was investigated. The kinetics of the process were investigated by soft XAS and it was revealed that low concentrations of Co^{2+} in the solution stabilize the catalytically active Co(Fe) sites [117].

8. Layered Double Hydroxide (LDH)

LDH are emerging catalyst materials with inner layer water molecules and higher anion exchange capacity. They have been extensively used as electrocatalytic materials owing to their high specific surface area, environmental friendliness, lower cost, and non-toxicity [118]. A kind of LDH itself may become photocatalysts for water splitting. The electronic properties, such as band structure, bandgap energy (Eg), density of states (DOS), and band edge placement for $M^{II}M^{III}$-LDHs (MI^{II} = Mg, Co, Ni and Zn; M^{III} = Al and Ga) were calculated by using the DFT + U method. The band structures of Mg- and Zn-based LDHs and Co- and Ni-based LDHs are responsive to ultraviolet ($Eg > 3.1$ eV) and visible light ($Eg < 3.1$ eV), respectively. The DOS calculations revealed that the photogenerated hole localizes on the surface hydroxyl group of LDHs, facilitating the oxidization of a water molecule without a long transportation route. The band edge placements of NiGa-, CoAl-, ZnAl-, and NiAl-LDHs have a driving force (0.965 eV, 0.836 eV, 0.667 eV, and 0.426 eV, respectively), toward oxygen evolution. In the experimental observations, only CoAl-LDH was an efficient oxygen evolution photocatalyst, agreeing well with the theoretical prediction [119].

For NiFe-LDH and Ni-LDH, the critical role of superficial oxygen vacancies in enhancing electronic transport was discussed based on the electrochemical analysis by correlating with electrocatalytic activities [120]. The in situ conversion process to yield a monolayer of $Ni(OH)_2$ on electrodes was presented and the dynamic active site of the monolayer promoted the OER process. Doping with Co caused the oscillation of Ni and Co valence states in NiCo hydroxide. This study defined an in situ conversion process to yield monolayer LDH and a fundamental understanding of the origin of the active sites in monolayer LDHs for the OER [121]. Direct spectroscopic evidence for the different active sites in Fe-free and Fe-containing Ni oxides was reported for ultrathin LDH samples. ^{18}O-labeling experiments in combination with in situ Raman spectroscopy were employed to probe the role of lattice oxygen as well as an active oxygen species, $NiOO^-$, in the catalysts. It was found that lattice oxygen is involved in the OER for Ni and NiCo-LDHs, but not for NiFe and NiCoFe-LDHs. Moreover, $NiOO^-$ is a precursor to oxygen for Ni and NiCo-LDHs, but not for NiFe and NiCoFe-LDHs [122]. For M-doped Ni-based LDH (M = Ni, Co, and Fe), the OER mechanism was investigated theoretically for the reaction processes of AEM, LOM, and IMOC (= intramolecular oxygen coupling) mechanism. Theory predicted overpotential and Tafel slopes, and the findings were in agreement with the observation. As a result, depending on the applied potential, the reaction mechanism changed [123]. In addition to electrocatalysts, NiFe-LDH may be used as the flexible electrode of Zinc-Air batteries [124].

For the Cu-NiFe-LDH electrocatalyst, a novel magnetic Fe^{III} site spin-splitting strategy was suggested [125]. The electronic structure and spin states of the Fe^{IIII} sites are effectively induced by the Jahn–Teller effect of Cu^{2+}. The theoretical calculations and operando ATR FTIR revealed that the facilitation for the O–O bond formation accelerated the production of O from OH and improved the OER activity [125]. For as-prepared sulfated Co-NiFe-LDH nanosheets, the kinetic energy barrier of the O–O coupling is significantly reduced. The formation of M-OOH on the active site at low overpotential was directly confirmed in 1 M KOH solution by in situ Raman and charge transfer fitting results. In a weakly alkaline environment of 0.1 M KOH, a sequential proton–electron transfer mechanism replaces the concerted proton–electron transfer mechanism, and the proton transfer step becomes the rate-determining step (RDS) as illustrated in **Figure 12** [126].

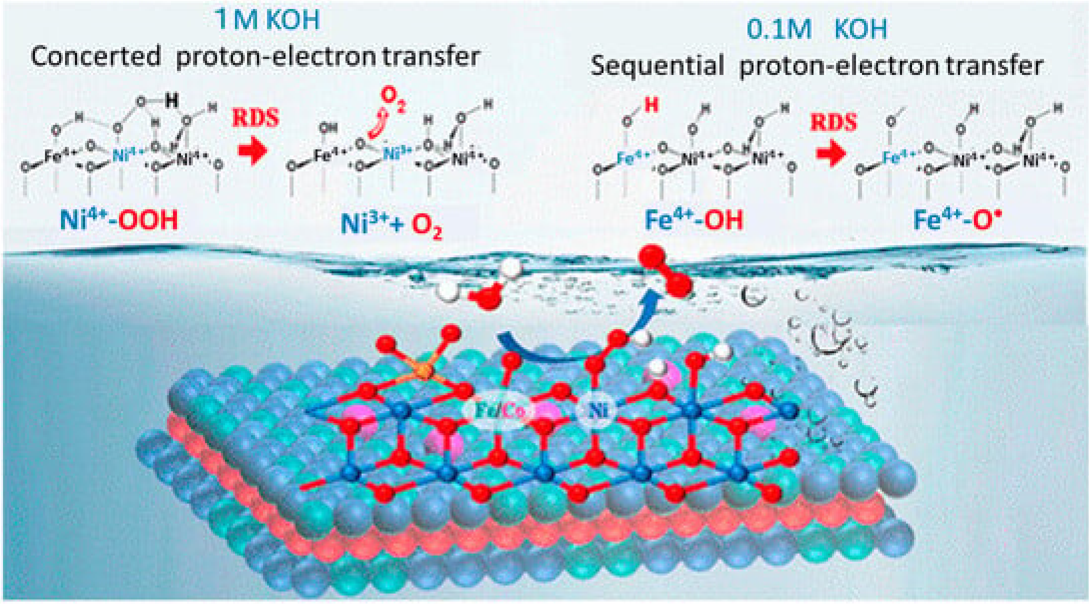

Figure 12. For Co-NiFe-LDH nanosheet, weakening alkaline concentration changes rate-determining step (RDS) from the release of O_2 to the oxo radical formation. Reproduced from *ACS Nano* **2023** [126] with permission from the American Chemical Society.

A Pt-induced NiFe-LDH (Pt-NiFe LDH) nanosheet was synthesized and large current density electrodes could be achieved in OER as well as HER [127]. At NiO/NiFe-LDH, the adsorption energy of *OH and *OOH can be adjusted independently, so as to bypass the scaling relationship and achieve high catalytic performance [128]. ZnO nanoparticles are uniformly distributed on the NiFe-LDH nanoflowers, which are prepared uniformly on the three-dimensional porous Ni foam. The active sites changed from Fe cations to Ni cations during OER and the OER dynamics were significantly improved [129]. The hierarchical bimetal nitride/hydroxide (NiMoN/NiFe LDH) array exhibits the industrially required current density. In situ electrochemical spectroscopy reveals that a hetero interface facilitates dynamic structure evolution to optimize the electronic structure. Operando EIS measurement implied the accelerated OER kinetics and intermediate evolution due to fast charge transport. For the OER mechanism, the combination of theoretical and experimental studies revealed that as-activated NiMoN/NiFe-LDH follows an LOM process with accelerated kinetics [130].

NiFe LDH@Ni_3S_2 heterostructure as an efficient bifunctional electrocatalyst for overall water splitting was prepared. Three-dimensional porous heterostructure arrays caused good electrocatalytic activity with a low Tafel slope [131]. By incorporating a semiconductor CdS/CdSe-MoS_2 and NiFe-LDH for the OER, the as-prepared photoelectrode required a potential lower than the theoretical water splitting potential. Operando XAS measurements revealed that the formation of highly oxidized Ni species under illumination provides large photocurrent gains [132]. Hetero structures of LDH with graphitic carbon nitride (g-C_3N_4) stand as promising photo- and electro-catalysts for water oxidation and reduction. Mechanisms involved in electrocatalytic, photocatalytic, and photoelectrocatalytic water splitting processes were reviewed with the necessary insights on the material [133]. By taking CuTi-LDH@g-C_3N_4 and $Bi_2O_2CO_3$/NiFe-LDH@g-C_3N_4 as examples, the importance of heterojunctions and interfacial chemistry in the water-splitting mechanism was explained in detail [133].

References

1. Wang, D.; Sheng, T.; Chen, J.; Wang, H.-F.; Hu, P. Identifying the key obstacle in photocatalytic oxygen evolution on rutile TiO2. Nat. Catal. 2018, 1, 291–299.
2. Li, B.; Wu, S.; Gao, X. Theoretical calculation of a TiO2-based photocatalyst in the field of water splitting: A review. Nanotechnol. Rev. 2020, 9, 85.
3. Malik, A.S.; Fredin, L.A. Unraveling the water oxidation mechanism on a stoichiometric and reduced rutile TiO2(100) surface using first-principles calculations. J. Phys. Chem. C 2023, 127, 3444–3451.

4. Nosaka, Y.; Nosaka, A.Y. Generation and detection of reactive oxygen species in photocatalysis. Chem. Rev. 2017, 117, 11302–11336.
5. Nosaka, Y.; Nosaka, A. Introduction to Photocatalysis: From Basic Science to Applications; Royal Society of Chemistry: Cambridge, UK, 2016; 272p.
6. Kakuma, Y.; Nosaka, A.Y.; Nosaka, Y. Difference of TiO2 photocatalytic mechanism between rutile and anatase studied by the detection of active oxygen and surface species in water. Phys. Chem. Chem. Phys. 2015, 17, 18691–18698.
7. Li, F.; Chen, J.-F.; Gong, X.-Q.; Hu, P.; Wang, D. Subtle structure matters: The vicinity of surface Ti5C cations alters the photooxidation behaviors of anatase and rutile TiO2 under aqueous environments. ACS Catal. 2022, 12, 8242–8251.
8. Nosaka, Y. Water photo-oxidation over TiO2—History and reaction mechanism. Catalysts 2022, 12, 1557.
9. Nakamura, R.; Nakato, Y. Primary intermediates of oxygen photoevolution reaction on TiO2 (rutile) particles, revealed by in situ FTIR absorption and photoluminescence measurements. J. Am. Chem. Soc. 2004, 126, 1290–1298.
10. Nakamura, R.; Okamura, T.; Ohashi, N.; Imanishi, A.; Nakato, Y. Molecular mechanisms of photoinduced oxygen evolution, PL emission, and surface roughening at atomically smooth (110) and (100) n-TiO2 (rutile) surfaces in aqueous acidic solutions. J. Am. Chem. Soc. 2005, 127, 12975–12983.
11. Nakamura, R.; Imanishi, A.; Murakoshi, K.; Nakato, Y. In situ FTIR studies of primary intermediates of photocatalytic reactions on nanocrystalline TiO2 films in contact with aqueous solutions. J. Am. Chem. Soc. 2003, 125, 7443–7450.
12. Zhuang, Y.-B.; Cheng, J. Deciphering the anomalous acidic tendency of terminal water at rutile(110)–water interfaces. J. Phys. Chem. C 2023, 127, 10532–10540.
13. Kudo, A.; Miseki, Y. Heterogeneous photocatalyst materials for water splitting. Chem. Soc. Rev. 2009, 38, 253–278.
14. Wang, Q.; Hisatomi, T.; Jia, Q.; Tokudome, H.; Zhong, M.; Wang, C.; Pan, Z.; Takata, T.; Nakabayashi, M.; Shibata, N.; et al. Scalable water splitting on particulate photocatalyst sheets with a solar-to-hydrogen energy conversion efficiency exceeding 1. Nat. Mater 2016, 15, 611–615.
15. Rather, R.A.; Mehta, A.; Lu, Y.; Valant, M.; Fang, M.; Liu, W. Influence of exposed facets, morphology and hetero-interfaces of BiVO4 on photocatalytic water oxidation: A review. Int. J. Hydrogen Energy 2021, 46, 21866–21888.

16. Ma, Y.; Pendlebury, S.R.; Reynal, A.; Formal, F.L.; Durrant, J.R. Dynamics of photogenerated holes in undoped BiVO4 photoanodes for solar water oxidation. Chem. Sci. 2014, 5, 2964–2973.
17. Abdellaoui, I.; Islam, M.M.; Remeika, M.; Higuchi, Y.; Kawaguchi, T.; Harada, T.; Budich, C.; Maeda, T.; Wada, T.; Ikeda, S.; et al. Photocarrier recombination dynamics in BiVO4 for visible light-driven water oxidation. J. Phys. Chem. C 2020, 124, 3962–3972.
18. Tran-Phu, T.; Fusco, Z.; Bernardo, I.D.; Lipton-Duffin, J.; Toe, C.Y.; Daiyan, R.; Gengenbach, T.; Lin, C.-H.; Bo, R.; Nguyen, H.T.; et al. Understanding the role of vanadium vacancies in BiVO4 for efficient photoelectrochemical water oxidation. Chem. Mater. 2021, 33, 3553–3565.
19. Walsh, A.; Yan, Y.; Huda, M.N.; Al-Jassim, M.M.; Wei, S.-H. Band edge electronic structure of BiVO4: Elucidating the role of the Bi s and V d orbitals. Chem. Mater. 2009, 21, 547–551.
20. Hu, J.; Zhao, X.; Chen, W.; Su, H.; Chen, Z. Theoretical insight into the mechanism of photoelectrochemical oxygen evolution reaction on BiVO4 anode with oxygen vacancy. J. Phys. Chem. C 2017, 121, 18702–18709.
21. Liu, G.; Li, F.; Zhu, Y.; Lia, J.L.; Sun, L. Cobalt doped BiVO4 with rich oxygen vacancies for efficient photoelectrochemical water oxidation. RSC Adv. 2020, 10, 28523–28526.
22. Liu, T.; Liu, R.; Li, Q.; Yang, J. Theoretical insight into the role of defects and facets in the selectivity of products in water oxidation over bismuth vanadate (BiVO4). ACS Sustain. Chem. Eng. 2020, 8, 1980–1988.
23. Wang, W.; Strohbeen, P.J.; Lee, D.; Zhou, C.; Kawasaki, J.K.; Choi, K.-S.; Liu, M.; Galli, G. The role of surface oxygen vacancies in BiVO4. Chem. Mater. 2020, 32, 2899–2909.
24. Steinitz-Eliyahu, R.; Hernangómez-Pérez, D.; Hegner, F.S.; Nikačević, P.; López, N.; Refaely-Abramson, S. Mixed excitonic nature in water-oxidized BiVO4 surfaces with defects. Phys. Rev. Mater. 2022, 6, 065402.
25. Huang, M.; He, W.; Xu, Z.; Zhu, H. Enhanced catalytic mechanism of twin-structured BiVO4. J. Phys. Chem. Lett. 2021, 12, 10610–10615.
26. Nikačević, P.; Hegner, F.S.; Galán-Mascarós, J.R.; López, N. Influence of oxygen vacancies and surface facets on water oxidation selectivity toward oxygen or hydrogen peroxide with BiVO4. ACS Catal. 2021, 11, 13416–13422.
27. Park, H.S.; Leonard, K.C.; Bard, A.J. Surface interrogation scanning electrochemical microscopy (SISECM) of photoelectrochemistry at a W/Mo-BiVO4 semiconductor electrode. J. Phys. Chem. C 2013, 117, 12093–12102.
28. Nakabayashi, Y.; Nishikawa, M.; Saito, N.; Terashima, C.; Fujishima, A. Significance of hydroxyl radical in photoinduced oxygen evolution in water on monoclinic bismuth vanadate. J. Phys. Chem. C 2017, 121, 25624–25631.

29. Nakabayashi, Y.; Suzuki, N.; Terashima, C.; Fujishima, A. In situ infrared analysis for the process of water photo-oxidation on monoclinic bismuth vanadate. J. Phys. Chem. C 2021, 125, 18579–18587.
30. Sun, Q.; Ren, K.; Qi, L. Boosting the performance of BiVO4 photoanodes by the simultaneous introduction of oxygen vacancies and cocatalyst via photoelectrodeposition. ACS Appl. Mater. Interfaces 2022, 14, 37833–37842.
31. Pan, L.; Wu, J.; Xu, X.; Lv, F.; Chen, Y.; Guo, L. Photoelectrochemical performance of bismuth vanadate photoanode for water splitting under concentrated light irradiation. Int. J. Hydrogen Energy 2023, 48, 13479–13488.
32. Majumder, S.; Su, X.; Kim, K.H. Effective strategy of incorporating Co3O4 as a co-catalyst onto an innovative BiVO4/Fe2TiO5 core-shell heterojunction for effective photoelectrochemical water-splitting application. Surf. Interfaces. 2023, 39, 102936.
33. Avcıoğlu, C.; Avcıoğlu, S.; Bekheet, M.F.; Gurlo, A. Photocatalytic overall water splitting by SrTiO3: Progress report and design strategies. ACS Appl. Energy Mater. 2023, 6, 1134–1154.
34. Chen, X.; Choing, S.N.; Aschaffenburg, D.J.; Pemmaraju, C.D.; Prendergast, D.; Cuk, T. The formation time of Ti–O• and Ti–O•–Ti radicals at the n-SrTiO3/aqueous interface during photocatalytic water oxidation. J. Am. Chem. Soc. 2017, 139, 1830–1841.
35. Chen, X.; Aschaffenburg, D.J.; Cuk, T. Selecting between two transition states by which water oxidation intermediates decay on an oxide surface. Nat. Catal. 2019, 2, 820–827.
36. Vinogradov, I.; Singh, S.; Lyle, H.; Paolino, M.; Mandal, A.; Rossmeisl, J.; Cuk, T. Free energy difference to create the M-OH• intermediate of the oxygen evolution reaction by time-resolved optical spectroscopy. Nat. Mater. 2022, 21, 88–94.
37. Lyle, H.; Singh, S.; Magnano, E.; Nappini, S.; Bondino, F.; Yazdi, S.; Cuk, T. Assessing and quantifying thermodynamically concomitant degradation during oxygen evolution from water on SrTiO3. ACS Catal. 2023, 13, 8206–8218.
38. Chen, T.; Ding, Q.; Wang, X.; Feng, Z.; Li, C. Mechanistic studies on photocatalytic overall water splitting over Ga2O3-based photocatalysts by operando MS-FTIR spectroscopy. J. Phys. Chem. Lett. 2021, 12, 6029–6033.
39. Zhou, X.; Hensen, E.J.M.; van Santen, R.A.; Li, C. DFT simulations of water adsorption and activation on low-index α-Ga2O3 surfaces. Chem. Eur. J. 2014, 20, 6915–6926.
40. Wang, Q.; Nakabayashi, M.; Hisatomi, T.; Sun, S.; Akiyama, S.; Wang, Z.; Pan, Z.; Xiao, X.; Watanabe, T.; Yamada, T.; et al. Oxysulfide photocatalyst for visible-light-driven overall water splitting. Nat. Mater. 2019, 18, 827–832.

41. Yu, H.; Ge, J. Recent advances in Ru-based electrocatalysts toward acid electrochemical water oxidation. Curr. Opinion Electrochem. 2023, 39, 101296.
42. Raman, A.S.; Vojvodic, A. Providing atomistic insights into the dissolution of rutile oxides in electrocatalytic water splitting. J. Phys. Chem. C 2022, 126, 922–932.
43. Liu, S.; Chang, Y.; He, N.; Zhu, S.; Wang, L.; Liu, X. Competition between lattice oxygen and adsorbate evolving mechanisms in rutile Ru-based oxide for the oxygen evolution reaction. ACS Appl. Mater. Interf. 2023, 15, 20563–20570.
44. Pavlovic, Z.; Ranjan, C.; Gao, Q.; van Gastel, M.; Schlögl, R. Probing the structure of a water-oxidizing anodic iridium oxide catalyst using Raman spectroscopy. ACS Catal. 2016, 6, 8098–8105.
45. Sivasankar, N.; Weare, W.W.; Frei, H. Direct observation of a hydroperoxide surface intermediate upon visible light-driven water oxidation at an Ir oxide nanocluster catalyst by rapid-scan FT-IR spectroscopy. J. Am. Chem. Soc. 2011, 133, 12976–12979.
46. Ooka, H.; Yamaguchi, A.; Takashima, T.; Hashimoto, K.; Nakamura, R. Efficiency of oxygen evolution on iridium oxide determined from the pH dependence of charge accumulation. J. Phys. Chem. C 2017, 121, 17873–17881.
47. Bozal-Ginesta, C.; Rao, R.R.; Mesa, C.A.; Liu, X.; Hillman, S.A.J.; Stephens, I.E.L.; Durrant, J.R. Redox-state kinetics in water-oxidation IrOX electrocatalysts measured by operando spectroelectrochemistry. ACS Catal. 2021, 11, 15013–15025.
48. Czioska, S.; Boubnov, A.; Escalera-López, D.; Geppert, J.; Zagalskaya, A.; Röse, P.; Saraçi, E.; Alexandrov, V.; Krewer, U.; Cherevko, S.; et al. Increased Ir−Ir interaction in iridium oxide during the oxygen evolution reaction at high potentials probed by operando spectroscopy. ACS Catal. 2021, 11, 10043–10057.
49. Ping, Y.; Nielsen, R.J.; Goddard III, W.A. The reaction mechanism with free energy barriers at constant potentials for the oxygen evolution reaction at the IrO2(110) surface. J. Am. Chem. Soc. 2017, 139, 149–155.
50. Binninger, T.; Doublet, M.-L. The Ir–OOOO–Ir transition state and the mechanism of the oxygen evolution reaction on IrO2(110). Energy Environ. Sci. 2022, 15, 2519–2528.
51. Liao, F.; Yin, K.; Ji, Y.; Zhu, W.; Fan, Z.; Li, Y.; Zhong, J.; Shao, M.; Kang, Z.; Shao, Q. Iridium oxide nanoribbons with metastable monoclinic phase for highly efficient electrocatalytic oxygen evolution. Nat. Commun. 2023, 14, 1248.
52. Xie, Y.; Chang, C.; Luo, F.; Yang, Z. Modulation in the d band of Ir by core–shell construction for robust water splitting electrocatalysts in acid. ACS Appl. Mater. Interfaces. 2023, 15, 20081–20088.

53. Reksten, A.H.; Thuv, H.; Seland, F.; Sunde, S. The oxygen evolution reaction mechanism at IrXRu1−XO2 powders produced by hydrolysis synthesis. J. Electroanal. Chem. 2018, 819, 547–561.
54. Rao, R.R.; Kolb, M.J.; Halck, N.B.; Pedersen, A.F.; Mehta, A.; You, H.; Stoerzinger, K.A.; Feng, Z.; Hansen, H.A.; Zhou, H.; et al. Towards identifying the active sites on RuO2(110) in catalyzing oxygen evolution. Energy Environ. Sci. 2017, 10, 2626–2637.
55. Liang, Q.; Bieberle-Hütter, A.; Brocks, G. Anti-ferromagnetic RuO2: A stable and robust OER catalyst over a large range of surface terminations. J. Phys. Chem. C 2022, 126, 1337–1345.
56. Stoerzinger, K.A.; Diaz-Morales, O.; Kolb, M.; Rao, R.R.; Frydendal, R.; Qiao, L.; Wang, X.R.; Halck, N.B.; Rossmeisl, J.; Hansen, H.A.; et al. Orientation-dependent oxygen evolution on RuO2 without lattice exchange. ACS Energy Lett. 2017, 2, 876–881.
57. Wang, Y.; Yang, R.; Ding, Y.; Zhang, B.; Li, H.; Bai, B.; Li, M.; Cui, Y.; Xiao, J.; Wu, Z.-S. Unraveling oxygen vacancy site mechanism of Rh-doped RuO2 catalyst for long-lasting acidic water oxidation. Nat. Commun. 2023, 14, 1412.
58. Shang, C.; Xiao, X.; Xu, Q. Coordination chemistry in modulating electronic structures of perovskite-type oxide nanocrystals for oxygen evolution catalysis. Coord. Chem. Rev. 2023, 485, 215109.
59. Hong, W.T.; Stoerzinger, K.A.; Lee, Y.-L.; Giordano, L.; Grimaud, A.; Johnson, A.M.; Hwang, J.; Crumlin, E.J.; Yange, W.; Shao-Horn, Y. Charge-transfer-energy-dependent oxygen evolution reaction mechanisms for perovskite oxides. Energy Environ. Sci. 2017, 10, 2190–2200.
60. Shi, Z.; Wang, X.; Ge, J.; Liu, C.; Xing, W. Fundamental understanding of the acidic oxygen evolution reaction: Mechanism study and state-of-the-art catalysts. Nanoscale 2020, 12, 13249–13275.
61. Lu, M.; Zheng, Y.; Hu, Y.; Huang, B.; Ji, D.; Sun, M.; Li, J.; Peng, Y.; Si, R.; Xi, P.; et al. Artificially steering electrocatalytic oxygen evolution reaction mechanism by regulating oxygen defect contents in perovskites. Sci. Adv. 2022, 8, eabq3563.
62. Peng, M.; Huang, J.; Zhu, Y.; Zhou, H.; Hu, Z.; Liao, Y.-K.; Lai, Y.-H.; Chen, C.-T.; Chu, Y.-H.; Zhang, K.H.L.; et al. Structural anisotropy determining the oxygen evolution mechanism of strongly correlated perovskite nickelate electrocatalyst. ACS Sustain. Chem. Eng. 2021, 9, 4262–4270.
63. Sun, Y.; Wu, C.-R.; Ding, T.-Y.; Gu, J.; Yan, J.-W.; Cheng, J.; Zhang, K.H.L. Direct observation of the dynamic reconstructed active phase of perovskite LaNiO3 for the oxygen evolution reaction. Chem. Sci. 2023, 14, 5906–5911.
64. Lee, S.; Kishore, M.R.A.; Kim, D.; Kang, H.; Chun, J.; Oh, L.S.; Park, J.H.; Kim, H.J.; Yoo, J.S.; Lim, E. Direct O–O coupling promoted the oxygen evolution reaction by dual active sites from

Ag/LaNiO3 interfaces. ACS Appl. Energy Mater. 2022, 5, 14658–14668.

65. Li, N.; Cai, L.; Gao, G.; Lin, Y.; Wang, C.; Liu, H.; Liu, Y.; Duan, H.; Ji, Q.; Hu, W.; et al. Operando direct observation of stable water-oxidation intermediates on Ca2−XIrO4 nanocrystals for efficient acidic oxygen evolution. Nano Lett. 2022, 22, 6988–6996.
66. Chen, H.; Shi, L.; Sun, K.; Zhang, K.; Liu, Q.; Ge, J.; Liang, X.; Tian, B.; Huang, Y.; Shi, Z.; et al. Protonated iridate nanosheets with a highly active and stable layered perovskite framework for acidic oxygen evolution. ACS Catal. 2022, 12, 8658–8666.
67. Yu, M.; Budiyanto, E.; Tgysgz, H. Principles of water electrolysis and recent progress in cobalt-, nickel-, and iron-based oxides for the oxygen evolution reaction. Angew. Chem. Int. Ed. 2022, 61, e202103824.
68. Han, J.; Guan, J. Multicomponent transition metal oxides and (oxy)hydroxides for oxygen evolution. Nano Res. 2023, 16, 1913–1966.
69. Wang, H.; Zhang, K.H.L.; Hofmann, J.P.; O'Shea, V.A.; Oropeza, F.E. The electronic structure of transition metal oxides for oxygen evolution reaction. J. Mater. Chem. A 2021, 9, 19465–19488.
70. Feng, Y.; Yang, H.; Wang, X.; Hu, C.; Jing, H.; Cheng, J. Role of transition metals in catalyst designs for oxygen evolution reaction: A comprehensive review. Int. J. Hydrogen Energy 2022, 47, 17946–17970.
71. Guo, T.; Li, L.; Wang, Z. Recent development and future perspectives of amorphous transition metal-based electrocatalysts for oxygen evolution reaction. Adv. Energy Mater. 2022, 12, 2200827.
72. Huang, C.-J.; Xu, H.-M.; Shuai, T.-Y.; Zhan, Q.-N.; Zhang, Z.-J.; Li, G.-R. A review of modulation strategies for improving catalytic performance of transition metal phosphides for oxygen evolution reaction. App. Catal. B Environ. 2023, 325, 122313.
73. Zhang, W.; Cao, R. Switching the O–O bond formation mechanism by controlling water activity. Chem 2021, 7, 1981–1992.
74. Takata, T.; Jiang, J.; Sakata, Y.; Nakabayashi, M.; Shibata, N.; Nandal, V.; Seki, K.; Hisatomi, T.; Domen, K. Photocatalytic water splitting with a quantum efficiency of almost unity. Nature 2020, 581, 411–414.
75. Wang, C.; Deng, R.; Guo, M.; Zhang, Q. Recent progress of advanced Co3O4-based materials for electrocatalytic oxygen evolution reaction in acid: From rational screening to efficient design. Int. J. Hydrogen Energy, 2023; in press.
76. Favaro, M.; Yang, J.; Nappini, S.; Magnano, E.; Toma, F.M.; Crumlin, E.J.; Yano, J.; Sharp, I.D. Understanding the oxygen evolution reaction mechanism on CoOX using operando ambient-pressure X-ray photoelectron spectroscopy. J. Am. Chem. Soc. 2017, 139, 8960–8970.

77. Moysiadou, A.; Lee, S.; Hsu, C.-S.; Chen, H.M.; Hu, X. Mechanism of oxygen evolution catalyzed by cobalt oxyhydroxide: Cobalt superoxide species as a key intermediate and dioxygen release as a rate-determining step. J. Am. Chem. Soc. 2020, 142, 11901–11914.
78. Lang, C.; Li, J.; Yang, K.R.; Wang, Y.; He, D.; Thorne, J.E.; Croslow, S.; Dong, Q.; Zhao, Y.; Prostko, G.; et al. Observation of a potential-dependent switch of water-oxidation mechanism on Co-oxide-based catalysts. Chem 2021, 7, 2101–2117.
79. Wang, S.; Jiang, Q.; Ju, S.; Hsu, C.-S.; Chen, H.M.; Zhang, D.; Song, F. Identifying the geometric catalytic active sites of crystalline cobalt oxyhydroxides for oxygen evolution reaction. Nat. Commun. 2022, 13, 6650.
80. Kang, W.; Wei, R.; Yin, H.; Li, D.; Chen, Z.; Huang, Q.; Zhang, P.; Jing, H.; Wang, X.; Li, C. Unraveling sequential oxidation kinetics and determining roles of multi-cobalt active sites on Co3O4 catalyst for water oxidation. J. Am. Chem. Soc. 2023, 145, 3470–3477.
81. Lin, Y.; Yu, L.; Tang, L.; Song, F.; Schlögl, R.; Heumann, S. In situ identification and time-resolved observation of the interfacial state and reactive intermediates on a cobalt oxide nanocatalyst for the oxygen evolution reaction. ACS Catal. 2022, 12, 5345–5355.
82. Zhou, D.; Li, F.; Zhao, Y.; Wang, L.; Zou, H.; Shan, Y.; Fu, J.; Ding, Y.; Duan, L.; Liu, M.; et al. Mechanistic regulation by oxygen vacancies in structural evolution promoting electrocatalytic water oxidation. ACS Catal. 2023, 13, 4398–4408.
83. Ren, X.; Ji, Y.; Zhai, Y.; Yuan, N.; Ding, J.; Li, Y.; Yan, J.; Liu, S.F. Self-assembled CoOOH on TiO2 for enhanced photoelectrochemical water oxidation. J. Energy Chem. 2021, 60, 512–521.
84. Yao, N.; Wang, G.; Jia, H.; Yin, J.; Cong, H.; Chen, S.; Luo, W. Intermolecular energy gap-induced formation of high-valent cobalt species in CoOOH surface layer on cobalt sulfides for efficient water oxidation. Angew. Chem. Int. Ed. 2022, 61, e202117178.
85. Li, L.-F.; Li, Y.-F.; Liu, Z.-P. Oxygen evolution activity on NiOOH catalysts: Four-coordinated Ni cation as the active site and the hydroperoxide mechanism. ACS Catal. 2020, 10, 2581–2590.
86. Wang, X.; Xi, S.; Huang, P.; Du, Y.; Zhong, H.; Wang, Q.; Borgna, A.; Zhang, Y.-W.; Wang, Z.; Wang, H.; et al. Pivotal role of reversible NiO6 geometric conversion in oxygen evolution. Nature 2022, 611, 702–708.
87. Wang, H.; Lu, S. Light inducing the geometric conversion of NiO6 to trigger a faster oxygen evolution reaction pathway: The coupled oxygen evolution mechanism. Energy Environ. Mater. 2023, 6, e12558.
88. Jiang, J.; Sun, F.; Zhou, S.; Hu, W.; Zhang, H.; Dong, J.; Jiang, Z.; Zhao, J.; Li, J.; Yan, W.; et al. Atomic-level insight into super-efficient electrocatalytic oxygen evolution on iron and vanadium co-doped nickel (oxy)hydroxide. Nat. Commun. 2018, 9, 2885.

89. Rao, R.R.; Corby, S.; Bucci, A.; García-Tecedor, M.; Mesa, C.A.; Rossmeisl, J.; Giménez, S.; Lloret-Fillol, J.; Stephens, I.E.L.; Durrant, J.R. Spectroelectrochemical analysis of the water oxidation mechanism on doped nickel oxides. J. Am. Chem. Soc. 2022, 144, 7622–7633.
90. Li, T.; Zhang, L.; Wang, J.; Zhang, X.; Zhang, L.; Wang, M.; Yan, C.; Tao Qian, T. Facilitating reconstruction of the hetero interface electronic structure by the enriched oxygen vacancy for the oxygen evolution reaction. Inorg. Chem. 2023, 62, 10504–10512.
91. Liu, J.; Xiao, J.; Wang, Z.; Yuan, H.; Lu, Z.; Luo, B.; Tian, E.; Waterhouse, G.I.N. Structural and electronic engineering of Ir-doped Ni-(oxy)hydroxide nanosheets for enhanced oxygen evolution activity. ACS Catal. 2021, 11, 5386–5395.
92. Tian, B.; Shin, H.; Liu, S.; Fei, M.; Mu, Z.; Liu, C.; Pan, Y.; Sun, Y.; Goddard III, W.A.; Ding, M. Double-exchange-induced in situ conductivity in nickel-based oxyhydroxides: An effective descriptor for electrocatalytic oxygen evolution. Angew. Chem. Int. Ed. 2021, 60, 16448–16456.
93. Xiong, Y.; He, P. A review on electrocatalysis for alkaline oxygen evolution reaction (OER) by Fe-based catalysts. J. Mater. Sci. 2023, 58, 2041–2067.
94. Zhang, Y.; Zhang, H.; Liu, A.; Chen, C.; Song, W.; Zhao, J. Rate-limiting O–O bond formation pathways for water oxidation on hematite photoanode. J. Am. Chem. Soc. 2018, 140, 3264–3269.
95. Righi, G.; Plescher, J.; Schmidt, F.-P.; Campen, R.K.; Fabris, S.; Knop-Gericke, A.; Schlögl, R.; Jones, T.E.; Teschner, D.; Piccinin, S. On the origin of multihole oxygen evolution in haematite photoanodes. Nat. Catal. 2022, 5, 888–899.
96. Adak, M.K.; Mallick, L.; Samanta, K.; Chakraborty, B. Slow O–H dissociation in the first-order oxygen evolution reaction kinetics on polycrystalline γ-FeO(OH). J. Phys. Chem. C 2023, 127, 154–168.
97. Gao, L.; Tang, C.; Liu, J.; He, L.; Wang, H.; Ke, Z.; Li, W.; Jiang, C.; He, D.; Cheng, L.; et al. Oxygen vacancy-induced electron density tuning of Fe3O4 for enhanced oxygen evolution catalysis. Energy Environ. Mater. 2021, 4, 392–398.
98. Ouyang, Q.; Cheng, S.; Yang, C.; Lei, Z. Ni, Co, and Yb cation Co-doping and defect engineering of FeOOH nanorods as an electrocatalyst for the oxygen evolution reaction. Inorg. Chem. 2023, 62, 1719–1727.
99. Li, C.; Chen, M.; Xie, Y.; Wang, H.; Jia, L. Boosting photoelectrochemical water splitting of bismuth vanadate photoanode via novel co-catalysts of amorphous manganese oxide with variable valence states. J. Colloid. Interf. Sci. 2023, 636, 103–112.
100. Zahran, Z.N.; Mohamed, E.A.; Naruta, Y. Kinetic and mechanism of heterogeneous water oxidation by α-Mn2O3 sintered on FTO electrode. ACS Catal. 2016, 6, 4470–4476.

101. Mousazade, Y.; Mohammadi, M.R.; Chernev, P.; Bikas, R.; Song, Z.; Lis, T.; Dau, H.; Najafpour, M.M. Water oxidation by a manganese–potassium cluster: Mn oxide as a kinetically dominant “true” catalyst for water oxidation. Catal. Sci. Technol. 2018, 8, 4390–4398.
102. Seo, H.; Park, S.; Cho, K.H.; Choi, S.; Ko, C.; Randriamahazaka, H.; Nam, K.T. Complex impedance analysis on charge accumulation step of Mn3O4 nanoparticles during water oxidation. ACS Omega 2021, 6, 18404–18413.
103. Yoon, S.; Seo, H.; Jin, K.; Kim, H.G.; Lee, S.-Y.; Jo, J.; Cho, K.H.; Ryu, J.; Yoon, A.; Kim, Y.-W.; et al. Atomic reconstruction and oxygen evolution reaction of Mn3O4 nanoparticles. J. Phys. Chem. Lett. 2022, 13, 8336–8343.
104. Zhang, B.; Daniel, Q.; Fan, L.; Liu, T.; Meng, Q.; Sun, L. Identifying MnVII-oxo species during electrochemical water oxidation by manganese oxide. iScience 2018, 4, 144–152.
105. Wang, Y.; Sharma, A.; Duong, T.; Arandiyan, H.; Zhao, T.; Zhang, D.; Su, Z.; Garbrecht, M.; Beck, F.J.; Karuturi, S.; et al. Direct solar hydrogen generation at 20% efficiency using low-cost materials. Adv. Energy Mat. 2021, 11, 2101053.
106. Zhang, J.; Winkler, J.R.; Gray, H.B.; Hunter, B.M. Mechanism of nickel−iron water oxidation electrocatalysts. Energy Fuels 2021, 35, 19164–19169.
107. Yang, Y.; Du, X.; Wang, S.; Zhao, K.; Wang, L.; Qi, Z.; Yang, W.; Hao, J.; Shi, W. Cation transport effect on nickel iron oxyhydroxide electrodes in the oxygen evolution reaction. Ind. Eng. Chem. Res. 2022, 61, 16702–16710.
108. Acharya, P.; Manso, R.H.; Hoffman, A.S.; Bakovic, S.I.P.; Kékedy-Nagy, L.; Bare, S.R.; Chen, J.; Greenlee, L.F. Fe coordination environment, Fe-incorporated Ni(OH) phase, and metallic core are key structural components to active and stable nanoparticle catalysts for the oxygen evolution reaction. ACS Catal. 2022, 12, 1992–2008.
109. Qian, H.; Wei, J.; Yu, C.; Tang, F.; Jiang, W.; Xia, D.; Gan, L. In situ quantification of the active sites, turnover frequency, and stability of Ni–Fe (oxy)hydroxides for the oxygen evolution reaction. ACS Catal. 2022, 12, 14280–14289.
110. Avcı, O.N.; Sementa, L.; Fortunelli, A. Mechanisms of the oxygen evolution reaction on NiFe2O4 and CoFe2O4 inverse-spinel oxides. ACS Catal. 2022, 12, 9058–9073.
111. Deng, H.; Jiang, H.; Wang, K.; Wang, Z.; Wang, B.; Zhou, Z.; Li, J. Coupling the vanadium-induced amorphous/crystalline NiFe2O4 with phosphide heterojunction toward active oxygen evolution reaction catalysts. Nanotechnol. Rev. 2022, 11, 3165–3173.
112. Schoen, M.A.W.; Calderon, O.; Randell, N.M.; Jimenez-Villegas, S.; Daly, K.M.; Chernikov, R.; Trudel, S. Local structural changes in polyamorphous (Ni,Fe)O electrocatalysts suggest a dual-site oxygen evolution reaction mechanism. J. Mater. Chem. A 2021, 9, 13252–13262.

113. Sugawara, Y.; Kamata, K.; Ishikawa, A.; Tateyama, Y.; Yamaguchi, T. Efficient oxygen evolution electrocatalysis on CaFe2O4 and its reaction mechanism. ACS Appl. Energy Mater. 2021, 4, 3057–3066.
114. Zheng, J.; Peng, X.; Xu, Z.; Gong, J.; Wang, Z. Cationic defect engineering in spinel NiCo2O4 for enhanced electrocatalytic oxygen evolution. ACS Catal. 2022, 12, 10245–10254.
115. Li, A.; Kong, S.; Guo, C.; Ooka, H.; Adachi, K.; Hashizume, D.; Jiang, Q.; Han, H.; Xiao, J.; Nakamura, R. Enhancing the stability of cobalt spinel oxide towards sustainable oxygen evolution in acid. Nat. Catal. 2022, 5, 109–118.
116. Zhang, B.; Wang, L.; Cao, Z.; Kozlov, S.M.; de Arquer, F.P.G.; Dinh, C.T.; Li, J.; Wang, Z.; Zheng, X.; Zhang, L.; et al. High-valence metals improve oxygen evolution reaction performance by modulating 3d metal oxidation cycle energetics. Nat. Catal. 2020, 3, 985–992.
117. Simondson, D.; Chatti, M.; Bonke, S.A.; Tesch, M.F.; Golnak, R.; Xiao, J.; Hoogeveen, D.A.; Cherepanov, P.V.; Gardiner, J.L.; Tricoli, A.; et al. Stable acidic water oxidation with a cobalt–iron–lead oxide catalyst operating via a cobalt-selective self-healing mechanism. Angew. Chem. Int. Ed. 2021, 60, 15821–15826.
118. Karim, A.V.; Hassani, A.; Eghbali, P.; Nidheesh, P.V. Nanostructured modified layered double hydroxides (LDHs)-based catalysts: A review on synthesis, characterization, and applications in water remediation by advanced oxidation processes. Curr. Opinion Solid State and Mater. Sci. 2022, 26, 100965.
119. Xu, S.-M.; Pan, T.; Dou, Y.-B.; Yan, H.; Zhang, S.-T.; Ning, F.-Y.; Shi, W.-Y.; Wei, M. Theoretical and experimental study on MIIMIII -layered double hydroxides as efficient photocatalysts toward oxygen evolution from water. J. Phys. Chem. C 2015, 119, 18823–18834.
120. Zhang, H.; Wu, L.; Feng, R.; Wang, S.; Hsu, C.-S.; Ashfaq, Y.N.; Zhang, A.C.; Wu, H.; Chen, H.-M.; Zhang, W.; et al. Oxygen vacancies unfold the catalytic potential of NiFe-layered double hydroxides by promoting their electronic transport for oxygen evolution reaction. ACS Catal. 2023, 13, 6000–6012.
121. Kang, J.; Qiu, X.; Hu, Q.; Zhong, J.; Gao, X.; Huang, R.; Wan, C.; Liu, L.-M.; Duan, X.; Guo, L. Valence oscillation and dynamic active sites in monolayer NiCo hydroxides for water oxidation. Nat. Catal. 2021, 4, 1050–1058.
122. Lee, S.; Banjac, K.; Lingenfelder, M.; Hu, X. Oxygen isotope labeling experiments reveal different reaction sites for the oxygen evolution reaction on nickel and nickel iron oxides. Angew. Chem. Int. Ed. 2019, 58, 10295–10299.
123. Wang, Z.; Goddard III, W.A.; Xiao, H. Potential-dependent transition of reaction mechanisms for oxygen evolution on layered double hydroxides. Nat. Commun. 2023, 14, 4228.

124. Xu, J.; Li, Z.; Chen, D.; Yang, S.; Zheng, K.; Ruan, J.; Wu, Y.; Zhang, H.; Chen, J.; Xie, F.; et al. Active electrocatalyst in the oxygen evolution reaction and flexible zinc–air batteries. ACS Appl. Mater. Interfaces 2021, 13, 48774–48783.
125. Sun, Z.; Lin, L.; He, J.; Ding, D.; Wang, T.; Li, J.; Li, M.; Liu, Y.; Li, Y.; Yuan, M.; et al. Regulating the spin state of FeIII enhances the magnetic effect of the molecular catalysis mechanism. J. Am. Chem. Soc. 2022, 144, 8204–8213.
126. Qiao, C.; Usman, Z.; Wei, J.; Gan, L.; Hou, J.; Hao, Y.; Zhu, Y.; Zhang, J.; Cao, C. Efficient O–O coupling at catalytic interface to assist kinetics optimization on concerted and sequential proton–electron transfer for water oxidation. ACS Nano 2023, 17, 12278–12289.
127. He, X.; Han, X.; Zhou, X.; Chen, J.; Wang, J.; Chen, Y.; Yu, L.; Zhang, N.; Li, J.; Wang, S.; et al. Electronic modulation with Pt-incorporated NiFe layered doublehydroxide for ultrastable overall water splitting at 1000 mA cm−2. App. Catal. B Environ. 2023, 331, 122683.
128. Gao, Z.-W.; Liu, J.-Y.; Chen, X.-M.; Zheng, X.-L.; Mao, J.; Liu, H.; Ma, T.; Li, L.; Wang, W.-C.; Du, X.-W. Engineering NiO/NiFe LDH intersection to bypass scaling relationship for oxygen evolution reaction via dynamic tridimensional adsorption of intermediates. Adv. Mater. 2019, 31, 1804769.
129. Luo, Y.; Wu, Y.; Wu, D.; Huang, C.; Xiao, D.; Chen, H.; Zheng, S.; Chu, P.K. NiFe-layered double hydroxide synchronously activated by heterojunctions and vacancies for the oxygen evolution reaction. ACS Appl. Mater. Interfaces 2020, 12, 42850–42858.
130. Zhai, P.; Wang, C.; Zhao, Y.; Zhang, Y.; Gao, J.; Sun, L.; Hou, J. Regulating electronic states of nitride/hydroxide to accelerate kinetics for oxygen evolution at large current density. Nat. Commun. 2023, 14, 1873.
131. Liang, X.; Li, Y.; Fan, H.; Deng, S.; Zhao, X.; Chen, M.; Pan, G.; Xiong, Q.; Xia, X. Bifunctional NiFe layered double hydroxide@Ni3S2 hetero structure as efficient electrocatalyst for overall water splitting. Nanotechnology 2019, 30, 484001.
132. Wu, Z.; Liu, X.; Li, H.; Sun, Z.; Cao, M.; Li, Z.; Fang, C.; Zhou, J.; Cao, C.; Dong, J.; et al. A semiconductor-electrocatalyst nano interface constructed for successive photoelectrochemical water oxidation. Nat. Commun. 2023, 14, 2574.
133. Guru, S.; Rao, G.R. Review—Strategic design of layered double hydroxides and graphitic carbon nitride heterostructures for photoelectrocatalytic water splitting applications. J. Electrochem. Soc. 2022, 169, 046515.

Retrieved from https://encyclopedia.pub/entry/history/show/118074